Lrrcc1 and Ccdc61 are conserved effectors of multiciliated cell function

Aude Nommick, Camille Boutin, Olivier Rosnet, Claire Schirmer, Elsa Bazellières, Virginie Thomé, Etienne Loiseau, Annie Viallat, Laurent Kodjabachian

Lrrcc1 and Ccdc61 are conserved effectors of multiciliated cell function

Aude Nommick[1,3], Camille Boutin[1], Olivier Rosnet[1,4], Claire Schirmer[1], Elsa Bazellières[1], Virginie Thomé[1], Etienne Loiseau[2], Annie Viallat[2], Laurent Kodjabachian[1,*]

1. Aix Marseille Univ, CNRS, IBDM, Turing Center for Living Systems, Marseille, France

2. Aix Marseille Univ, CNRS, CINaM, Turing Center for Living Systems, Marseille, France

3. Present address: Université de Paris, CNRS, Institut Jacques Monod, F-75006 Paris, France

4: Present address: Aix Marseille Univ, CNRS, INSERM, Institut Paoli-Calmettes, CRCM, Marseille, France

* corresponding author: laurent.kodjabachian@univ-amu.fr

Running title: Lrrcc1 and Ccdc61 in MCCs

Keywords: *Xenopus*, multiciliated cell, Lrrcc1, Ccdc61, centriole, polarity, cytoskeleton

Summary statement: This study highlights the importance of Lrrcc1 and Ccdc61 in *Xenopus* multiciliated cell organization. Furthermore, it establishes the role of MCCs in flushing out environmental pathogens from the skin.

Abstract

Ciliated epithelia perform essential functions across animal evolution, ranging from locomotion of marine organisms to mucociliary clearance of airways in mammals. These epithelia are composed of multiciliated cells (MCCs) harbouring myriads of motile cilia, which rest on modified centrioles called basal bodies (BBs), and beat coordinately to generate directed fluid flows. Thus, BB biogenesis and organization is central to MCC function. In basal eukaryotes, the coiled-coil domain proteins Lrrcc1 and Ccdc61 were shown to be required for proper BB construction and function. Here, we used the *Xenopus* embryonic ciliated epidermis to characterize Lrrcc1 and Ccdc61 in vertebrate MCCs. We found that they both encode BB components, localized proximally at the junction with striated rootlets. Knocking down either gene caused defects in BB docking, spacing, and polarization. Moreover, their depletion impaired the apical cytoskeleton, and altered ciliary beating. Consequently, cilia-powered fluid flow was greatly reduced in morphant tadpoles, which displayed enhanced mortality when exposed to pathogenic bacteria. This work illustrates how integration across organizational scales make elementary BB components essential for the emergence of the physiological function of ciliated epithelia.

Introduction

Multiciliated epithelia are composed of multiciliated cells (MCCs) harboring numerous motile cilia. Ciliary beating generates powerful strokes essential for a variety of physiological functions in animals (Meunier and Azimzadeh, 2016). In aquatic organisms of the *Lophotrochozoan* and *Echinodermata* phyla, coordinated MCC beating is required for locomotion, clearance and transport of particles, and for feeding of larvae. In vertebrates, MCCs produce external or internal fluid flows. In lungfish, the ciliated epidermis clears the animal of particles and settling organisms before hatching (Kemp, 1996). In amphibian embryos, several roles have been proposed for the ciliated epidermis: prevention of micro-organisms and debris from attaching to the epidermis, pre-hatching rotation and post-hatching gliding, respiratory gas exchange, movement of surface mucus films and transportation of chemical signals to the olfactory organs (Nokhbatolfoghahai et al., 2006). Which of those roles is carried out by MCCs of the *Xenopus* embryonic epidermis remains unclear, despite a recent wealth of mechanistic studies in this model (Boutin and Kodjabachian, 2019; Brooks and Wallingford, 2014). In mammals, among other functions, MCCs help circulation of the cerebrospinal fluid in the central nervous system, mucociliary clearance of pathogens and pollutants from airways, and transportation of gametes in genital tracts (Spassky and Meunier, 2017). Consequently, mutations in genes necessary for multiple cilia formation or beating cause familial syndromes characterized by severe chronic airway infections, and an elevated risk of infertility (Boon et al., 2014; Wallmeier et al., 2014). A precise multiscale organization of ciliary beating is required to establish a robust and directed flow at the surface of ciliated epithelia. At the cellular scale, all cilia must beat in the same direction, and at the tissue scale the beating direction must be coordinated between neighboring cells. The Planar Cell Polarity pathway plays a prominent role in the establishment and maintenance of cilia polarity, both at tissue and cellular scales

(Boutin et al., 2014; Chien et al., 2015; Mitchell et al., 2009; Park et al., 2008; Walentek et al., 2017).

Motile cilia of MCCs are built via a multistep process (Boutin and Kodjabachian, 2019; Spassky and Meunier, 2017). First, numerous centrioles must be produced and subsequently released in the cytoplasm (Al Jord et al., 2014; Zhao et al., 2013). Next, centrioles migrate and dock at the apical surface, where they acquire a regular distribution and a coordinated orientation (Herawati et al., 2016; Park et al., 2008; Werner et al., 2011). Finally, ciliary axonemes extend from docked centrioles, and metachronal waves of ciliary beating are initiated and subsequently reinforced by mechanical feedback from the flow, which refines the coordination of cilia polarity (Guirao et al., 2010; Mitchell et al., 2007). During their journey towards the surface, centrioles mature into basal bodies (BBs) by acquiring basal foot (BF) and rootlet appendages, which localize asymmetrically and are essential for cilia polarization (Meunier and Azimzadeh, 2016). In *Xenopus* epidermal MCCs, two different types of rootlets attach to the proximal end of BBs. The most prominent rootlet has a fan shape and is localized opposite to the BF, which itself is positioned distally on the BB. The second rootlet is much longer and thinner and dives into the cytoplasm (Zhang and Mitchell, 2015). These appendages confer an intrinsic polarity to BBs, which in mature MCCs reflects the direction of ciliary beating, with the BF pointing in the direction of the effective stroke.

MCC cilia formation and organization relies on close interactions between BBs and cytoskeletal elements (Boutin and Kodjabachian, 2019; Meunier and Azimzadeh, 2016). The transport and docking of centrioles/BBs to the apical surface is dependent on acto-myosin-based mechanisms (Boisvieux-Ulrich et al., 1990; Epting et al., 2015; Kulkarni et al., 2018; Lemullois et al., 1988; Miyatake et al., 2015; Park et al., 2008). Once docked, neighboring BBs are linked by subapical actin filaments and apical microtubules (MTs) emanating from rootlets and BFs, respectively. The geometrical network hence made ensures regular BB spacing and coordinated orientation

over the apical cell surface (Antoniades et al., 2014; Lemullois et al., 1988; Park et al., 2006; Werner et al., 2011; Yasunaga et al., 2015). Chemical interference with actin or MT networks leads to BB disorganization and impaired ciliary function (Herawati et al., 2016; Werner et al., 2011). Reciprocally, depletion of specific centriolar components, which prevents the formation of appendages and/or preclude BB/cytoskeleton interactions, alter BB organization and ciliary function (Antoniades et al., 2014; Bustamante-Marin et al., 2019; Clare et al., 2014; Herawati et al., 2016; Kulkarni et al., 2018; Kunimoto et al., 2012; Turk et al., 2015; Walentek et al., 2016).

Lrrcc1 (Leucine rich repeat coiled-coil domain containing 1) and Ccdc61 (Coiled-coil domain-containing protein 61) are structural proteins, conserved from *Chlamydomonas* to human, which are involved in centriole appendage biogenesis and function, both at the centrosome and at ciliary BBs (Adams et al., 1985; Barenz et al., 2018; Basquin et al., 2019; Bengueddach et al., 2017; Hoops et al., 1984; Muto et al., 2008; Ochi et al., 2020; Pizon et al., 2020; Silflow et al., 2001; Wright et al., 1983). In MCCs of the planarian epidermis, Lrrcc1 (Vfl1) and Ccdc61 (Vfl3) depletion causes structural BB defects, thus perturbing cilia orientation, and altering the direction of locomotion (Basquin et al., 2019). The functional importance of Lrrcc1 and Ccdc61 in vertebrate MCCs remains unknown, although Ccdc61 was recently reported to associate with BBs in *Xenopus* MCCs (Ochi et al., 2020). Here, we used the *Xenopus laevis* ciliated epidermis as a model to shed light on this issue. We decided to comparatively study Lrrcc1 and Ccdc61, based on their shared biological functions in *Chlamydomonas* and *Schmidtea* (Adams et al., 1985; Basquin et al., 2019; Hoops et al., 1984; Wright et al., 1983), and their reported physical interaction in an unbiased human proteomic screen (Hein et al., 2015). In *Xenopus*, MCCs are specified deeply, in the inner cellular layer of the epidermis before intercalating at regular intervals into the outer cellular layer (Chuyen et al., 2021; Collins et al., 2021; Collins et al., 2020; Deblandre et al., 1999; Stubbs et al., 2006; Werner et al.,

2014). BB synthesis is initiated while MCCs are still in the inner epidermal layer (Klos Dehring et al., 2013; Revinski et al., 2018); BB docking, distribution, orientation and ciliogenesis are completed when MCCs have radially intercalated and expanded their apical surface (Chung et al., 2014; Kulkarni et al., 2021; Sedzinski et al., 2016).

We report here that Lrrcc1 and Ccdc61 are both associated to *Xenopus* MCC centrioles, with a preferential localization near the basis of ciliary rootlets in mature MCCs. We found that knocking down either gene impacts ciliated epithelium biogenesis at multiple scales. At the organelle scale, Ccdc61 is required for rootlet association of Pericentrin (Pcnt), that we characterize as a novel marker of this appendage in *Xenopus* BBs. At the cellular scale, we show that Lrrcc1 and Ccdc61 are required for proper organization of BBs. In addition, MCCs depleted for either gene present important defects in apical cytoskeleton organization. Finally, at the scale of the embryo, Lrrcc1 and Ccdc61 knock-down revealed their importance for the generation of superficial fluid flows and the resistance to opportunistic pathogens. This study bridges multiple scales of analysis to reveal how intracellular disorganization of MCCs can impair the physiology of the whole organism.

Results

Lrrcr1 and Ccdc61 are associated to centrioles and basal bodies in MCCs

Single cell RNA sequencing (scRNA-seq) of *Xenopus tropicalis* embryos revealed that *lrrcc1* and *ccdc61* are specifically expressed in ciliated epidermal cells from gastrula stages onwards (Briggs et al., 2018), and both genes were found to be activated by the Multicilin/E2F4/5 complex, which is known to be necessary and sufficient for vertebrate MCC differentiation (Ma et al., 2014). We used whole mount *in situ* hybridization to analyze the localization of *lrrcc1* and *ccdc61* transcripts in *Xenopus laevis* embryos. At early tailbud stage 20, both genes

displayed a "salt and pepper" pattern typical of epidermal MCCs (Fig. S1A). Double fluorescent *in situ* hybridization confirmed expression in MCCs marked by *α-tubulin* (Fig. S1B).

Next, we used fluorescent immunostaining to analyze the distribution by confocal microscopy of the endogenous Lrrcc1 and Ccdc61 proteins at different time points during MCC differentiation. At stage 18, when released centrioles start migrating towards the apical surface, both proteins appeared closely associated to individual neo-centrioles marked by Centrin (Fig. 1A,G). At stage 31, both Lrrcc1 and Ccdc61 were found associated to mature BBs docked at the apical surface (Fig. 1B, H). The Lrrcc1 signal was systematically located on one side of Centrin-positive BBs. In zoomed-in orthogonal view, the signal flanked the BB and extended towards the cytoplasm (Fig. 1B). The Ccdc61 signal overlapped considerably more with Centrin in both top and lateral views (Fig. 1H). To assess with more precision Lrrcc1 and Ccdc61 localization, we analyzed their distribution in 3D, relative to Centrin and γ-Tubulin, which is known to localize to the BF cap in MCCs (Clare et al., 2014; Hagiwara et al., 2000). On a top view, Centrin appeared as a single dot (Fig. 1E,K). Unexpectedly, two pools of γ-Tubulin were detected adjacent to the BB. The first pool appeared as a dot with strong intensity juxtaposed to the BB core. A lateral view revealed that this dot was located at a depth similar to that of the BB (Fig. 1E,K), thus corresponding to the γ-Tubulin previously described at the BF. In contrast, the second pool of γ-Tubulin displayed a less intense signal, localized opposite to the BF with respect to the BB, and extended into the cytoplasm (Fig. 1E,K), in a position compatible with the fan-shaped rootlet described in *Xenopus* MCCs (Zhang and Mitchell, 2015). To further assess this possibility, we applied Centrin and γ-Tubulin immunostaining on embryos injected with Clamp-GFP, an accepted marker of the fan-shaped rootlet in *Xenopus* (Park et al., 2008). This analysis confirmed that the weaker pool of γ-Tubulin is at the rootlet (Fig. S1C). 3D analysis revealed that the Lrrcc1 signal was localized adjacent to the rootlet pool of γ-Tubulin (Fig. 1E). A similar localization was observed in MCCs expressing an Lrrcc1-GFP

fusion construct (Fig. S1D,E). Triple staining with Centrin and Clamp-GFP revealed that the Lrrcc1 signal was concentrated at the junction between the BB and the rootlet (Fig. 1F). We note, however, that the Lrrcc1 signal detected below Centrin in uninjected MCCs (Fig. 1E), was strongly diminished in Clamp-GFP injected MCCs (Fig. 1F). This could reflect displacement of Lrrcc1 by Clamp-GFP, or reduced Lrrcc1 antibody accessibility. Triple staining with Centrin and Clamp-GFP revealed that the Ccdc61 signal was localized at the junction between the BB and the rootlet (Fig. 1L). Consistently, a Ccdc61-GFP fusion construct localized opposite to the BF pool of γ-Tubulin (Fig. S1F,G). A similar localization was recently reported for a Ccdc61-RFP fusion in *Xenopus* epidermal MCCs (Ochi et al., 2020).

We conclude that Lrrcc1 and Ccdc61 preferentially localize at the junction between the BB and the rootlets in mature epidermal MCCs of *Xenopus*.

Altogether these data suggest that Lrrcc1 and Ccdc61 are associated to epidermal MCC centrioles from the time of their release in the cytoplasm through the phases of docking, BB maturation, ciliary growth and maintenance.

Lrrcc1 and Ccdc61 depletion impairs centriole docking, spacing and orientation

The subcellular distribution of Lrrcc1 and Ccdc61 during MCC differentiation suggested that they could be involved in BB apical docking as well as distribution and orientation at the apical surface. To investigate this, we knocked down *lrrcc1* and *ccdc61* through injection in the presumptive epidermis of two independent morpholino antisense oligonucleotides (MOs) designed to block translation (MO-ATG) or splicing (MO-Spl) (Fig. S2A). The capacity of translation MOs to inhibit protein synthesis was verified both by Western blotting and immunofluorescence of endogenous or GFP-tagged proteins (Fig. S2B-G). We performed immunostaining at stage 31 to analyze BB organization in morphant MCCs. As previously described (Werner et al., 2011), BBs displayed a stereotypical organization in mature control

MCCs. They were all docked, quite evenly distributed at the apical surface and oriented in a coordinated manner (Fig. 2A, C, E). In contrast, Lrrcc1 and Ccdc61 knock-down drastically impaired centriole organization and morphant cells could be classified in two phenotypic categories. The first phenotypic class was characterized by clusters of centrioles stuck in the upper half of the cytoplasm (Fig. 2A, Fig. S3A). To quantify this defect, we analyzed the apico-basal (A-B) distribution of centrioles along the Z-axis of confocal stack acquisitions. In control cells, most centrioles localized within the first 1,6 µm below the apical cell surface (Fig. 2B). In contrast, in Lrrcc1-ATG and Ccdc61-ATG morphant cells most centrioles localized deeper, between 1,6 µm and 5.6 µm from the surface (Fig. 2B). Similar results were obtained with Lrrcc1-Spl and Ccdc61-Spl MOs (Fig. S3B). In the second phenotypic class, most centrioles properly localized at the apical surface, but displayed irregular spacing and a randomized orientation (Fig. 2C, E and Fig. S3C, E). To quantify BB spacing defects, we applied Delaunay triangulation between the centroids of docked centrioles and measured the area of the obtained triangles. In the control situation, the even distribution of BBs resulted in many triangles of similar area that tightly distributed around the median (Fig. 2C, D and Fig. S3C, D). In contrast, in morphant cells, variable distances between BBs resulted in a broader distribution of triangles around the median (Fig. 2C, D and Fig. S3C, D). We revealed BB orientation by immunostaining the BB core (Centrin) and the offset BF (intense γ-Tubulin spot), which allowed us to automatically extract orientation vectors and plot their circular distribution. In control cells, vector angles tightly distributed around the mean, indicating that BBs oriented in the same global direction. In Lrrcc1 and Ccdc61 morphant cells, the intense γ-Tubulin signal was largely preserved, suggesting that the integrity of the BF was maintained. However, vector angles were widely distributed around the mean, indicating a randomization of BB orientation (Fig. 2E and Fig. S3E). Accordingly, circular standard deviation values were significantly higher in morphants, as compared to control (Fig. 2F and Fig. S3F). The Rayleigh statistical

test also revealed a higher percentage of morphant MCCs, in which no significant mean vector could be defined, as compared to control (Fig. 2G and Fig. S3G).

In both Lrrcc1 and Ccdc61 morphant MCCs, cilia could be observed, suggesting that those proteins are not required for ciliary growth *per se* (Fig. S4). Importantly, for both genes and both types of MOs, docking, spacing and orientation phenotypes were rescued by co-injection of *lrrcc1* or *ccdc61* mRNA constructs lacking (*lrrcc1*), or silently mutated (*ccdc61*) on the MO-binding sequence (Fig. 2B, D, F, Fig. S3B, D, F and S5).

Altogether, these data show that Lrrcc1 and Ccdc61 are required for correct apical migration and/or docking of BBs, as well as for their proper planar distribution and orientation at the apical surface.

Ccdc61 is required for Pericentrin association to rootlet

Our localization and functional data suggested that Lrrcc1 and Ccdc61 could participate to the formation of rootlet appendages in *Xenopus* MCCs. To analyze this possibility, we performed TEM experiments on stage 31 MCCs from control and morphant embryos. The presence of centriole docking defects was used as a way to ascertain the morphant character of scored MCCs (Fig. 3B). Both fan-shape and thin rootlets could be observed in similar proportions in Lrrcc1 and Ccdc61 morphant cells, as compared to control (Fig. 3A, C). Whenever visible, rootlets did not present obvious structural or positioning defects.

Next, we looked for potential molecular defects of ciliary rootlets in morphant MCCs. In the course of an independent study about its role in MCC biogenesis (unpublished), we produced a polyclonal antibody against *Xenopus* Pcnt (Fig. S6A, B), which allowed us to uncover its association to ciliary rootlets. In stage 31 control cells, Pcnt immunostaining presented a dotted pattern, and was associated with Centrin and γ-Tubulin at the apical surface (Fig. 3D). 3D-analysis of the relative distribution of these proteins in individual BBs revealed that Pcnt was

located opposite to the strong BF-associated dot of γ-Tubulin, in a plane below Centrin. It was present as one or two dots emerging from the BB and extending towards the cytoplasm (Fig. 3D'). Pcnt association to rootlets was further confirmed by its co-localization with Clamp-GFP (Fig. 3E, E'). This series of tests revealed that in *Xenopus* epidermal MCCs, Pcnt specifically localizes at rootlets.

Next, we analyzed Pcnt signal in Lrrcc1 and Ccdc61 morphant embryos. To avoid immunostaining variability between different embryos, we compared Pcnt signal intensity within mosaic embryos. For Lrrcc1, no differences were observed between non-injected and morphant cells, which, however, clearly displayed randomized BB polarity (Fig. 3F, G). In contrast, a marked decrease of Pcnt signal was observed in Ccdc61 morphant cells, as compared to non-injected cells from the same embryos (Fig. 3F, G).

Altogether, these experiments suggest that Lrrcc1 and Ccdc61 are not essential for building rootlet appendages in *Xenopus* MCCs. However, Ccdc61 is required for association of the protein Pcnt to the rootlet, which could possibly affect rootlet function and MCC organization.

Lrrcc1 and Ccdc61 depletion disturbs apical cytoskeleton organization

BB organizational defects observed in Ccdc61 and Lrrcc1 morphant cells could be linked to defective apical cytoskeleton. To test this idea, we first analyzed F-actin networks in MCCs at stage 31. In control cells, we observed the stereotypical organization in apical and subapical networks that was previously described for mature MCCs (Werner et al., 2011). The apical actin network was organized like a grid surrounding each centriole, and the subapical network located just below was composed of short actin fibers that are known to connect neighboring BBs via their rootlets (Fig. 4A, A'). Both Lrrcc1 and Ccdc61 knockdown caused a global decrease of F-actin staining (Fig. 4D, E). When looking at individualized centrioles, a strong reduction of both apical and subapical F-actin was observed (Fig. 4B', C'). From these results,

we conclude that Lrrcc1 and Ccdc61 are, either directly or indirectly, involved in the assembly of the apical filamentous actin networks.

Next, we analyzed the apical MT network in mature MCCs. At stage 31, anti-α-Tubulin antibodies mainly revealed cilia, precluding the analysis of intracellular MT networks in mature MCCs (Fig. S7). To circumvent this limitation, we adopted a deciliation strategy to deplete cilia-associated signals and visualize intracellular MTs (Fig. S7). At stage 31, control cells were characterized by a highly organized apical MT network connecting BBs together (Fig. 5A, A'), similar to what has been reported by another method (Werner et al., 2011). In Lrrcc1 and Ccdc61 depleted-MCCs, intense α-Tubulin signals were found associated to clustered centrioles (Fig. 5B, B', D, D'). When looking at individualized BBs, MTs were clearly visible but the size and spatial organization of filaments appeared heterogeneous, as compared to control (Fig 5C, C', E, E'). These results suggest that Lrrcc1 and Ccdc61 are not necessary for apical MT network polymerization *per se*. Thus, the apparent MT network disorganization may be secondary to the loss of BB polarity.

Finally, we analyzed the apical intermediate filament (IF) network using the anti-cytokeratin C-11 antibody. At stage 18, we did not detect IFs inside or at the MCC surface, suggesting that they are not involved in centriole apical migration (Fig. 6A). At stage 31, IFs were organized into a dense grid surrounding each BB (Fig. 6B, B'), similar to what has been described in tracheal MCCs (Tateishi et al., 2017). Strikingly, IF organization was drastically affected in Lrrcc1 and Ccdc61 morphant cells. Overall, the lattice appeared much less dense and the annular organization of IF around BBs was lost (Fig. 6C, C', D, D'). This analysis suggests that Lrrcc1 and Ccdc61 are, directly or indirectly, involved in the establishment of the tight IF network in which BBs are embedded.

Altogether these analyses reveal that Lrrcc1 and Ccdc61 depletion has profound impacts on MCC apical cytoskeleton organization.

Lrrcc1 and Ccdc61 depletion reduces ciliary beating, impairs flow circulation and increases sensitivity to pathogen

The perturbed organization of BBs in morphant MCCs is expected to disturb the function of associated cilia, thereby affecting the production of fluid flow at the surface of the embryo. To address this issue, we first analyzed ciliary beating frequency by high-speed video-recording. As previously described, control MCCs performed synchronised and large amplitude effective and recovery strokes, characterized by the ability of cilia to extensively bend (Fig. 7A, and Movies 1 and 2)(Werner et al., 2011). In Lrrcc1 and Ccdc61 morphant embryos, we observed three levels of beating defaults: (i) low-amplitude, uncoordinated and disoriented beating, causing occasional collisions between cilia; (ii) cilia performing only small vibrations; (iii) extreme cases with totally immobile cilia (Fig. 7A, and Movies 1 and 2). Accordingly, the beating frequency, which was about 20 Hz for the control condition, decreased to lower values in a large majority of morphant MCCs (Fig. 7A). Next, we analyzed cilia-generated flow in the surrounding liquid, by live recording of visible dyed microspheres dispersed in the fluid, along the flanks of embryos at stage 31. In control condition, microspheres were moved by a robust flow and traveled the entire length of the embryo in approximately 12 seconds. In contrast, the flow was severely slowed down in Lrrcc1 and Ccdc61 morphant conditions, and the microspheres rarely reached the middle of the embryo after 12 seconds (Fig. 7B, C and Movie 3).

To address the impact of impaired ciliary flow on the physiology of morphant individuals, we analyzed their susceptibility to pathogen infection. Embryos were incubated for 72h with the opportunistic bacteria *Aeromonas Hydrophila* (Dubaissi et al., 2018), and their survival rate was recorded. Non-injected and GFP-injected embryos were used as controls. For both control conditions, an almost complete survival rate was observed independently of the presence or not

of bacteria (Fig. 7D). In absence of bacteria, Lrrcc1 and Ccdc61 morphant embryos displayed a slightly decreased survival rate as compared to control embryos. However, the presence of pathogenic bacteria strongly impacted the survival rate of morphants, starting from 24h of incubation. We confirmed by immunostaining that centrioles and cilia were disorganized in morphant embryos from the same experimental series (Fig. S8). This assay suggests that Lrrcc1 and Ccdc61 inactivation leads to a higher susceptibility of embryos to pathogen infection, likely due to reduced cilia-powered clearance.

Discussion

In this study, we report a role for Lrrcc1 and Ccdc61 in *Xenopus* epidermal MCC differentiation and function, extending their evolutionary conserved importance in ciliated cells to vertebrates. At the cellular scale, both Lrrcc1 and Ccdc61 are necessary for the migration and/or docking, spacing and polarization of BBs at the cell surface and for apical cytoskeleton organization. At a larger scale, both factors are necessary for cilia-powered superficial flow to help survival of the organism, when exposed to environmental pathogens.

Lrrcc1 and Ccdc61 proteins both contain coiled-coil domains, which are one of the most common structural motifs mediating protein–protein interactions. Search in the IntAct protein interaction database reveals that Lrrcc1 and Ccdc61 physically interact with multiple known factors related to centrosomes, cilia and MT organization or polymerization, among which 30% are actually shared (Table S1)(Hein et al., 2015). Moreover, 20/26 (Lrrcc1), and 12/23 (Ccdc61) of those interactors were found to be expressed in MCCs of *Xenopus tropicalis*, as revealed by scRNA-seq (Table S1)(Briggs et al., 2018). Together with their reported interaction, this information is consistent with Lrrcc1 and Ccdc61 shared localization and phenotypes, and suggest that these two factors belong to a common molecular network important for BB function in MCCs.

We show that Ccdc61 and Lrrcc1 associate to BBs early after their production and maintain this association in fully differentiated MCCs. The early association to neo-synthesized centrioles is compatible with a role in apical migration, which appears to be incomplete in Lrrcc1- and Ccdc61-deficient mature MCCs. Alternatively, apical migration may be unaffected, and defective docking may secondarily cause BBs to dive back into the cytoplasm. The distribution of Lrrcc1 and Ccdc61 at BBs is consistent with their observed requirement for correct MCC organization and function. This role is shared with Vfl1 (Lrrcc1) and Vfl3 (Ccdc61) orthologs, which are required to organize flagella/cilia in *Chlamydomonas*, *Paramecium* and planarians (Adams et al., 1985; Basquin et al., 2019; Bengueddach et al., 2017; Hoops et al., 1984; Wright et al., 1983). In all these species, these two factors are required for the proper construction of centriolar appendages. Based on our data and this literature, we propose that Lrrcc1 and Ccdc61 may be involved in rootlet appendage formation and/or function in *Xenopus* MCCs. In contrast to studies in these species, however, we did not detect major rootlet structural defects upon Lrrcc1 or Ccdc61 depletion, suggesting the existence of redundant mechanisms to build up *Xenopus* BB appendages.

From their place of birth to their final position at the apical surface, the relocation of centrioles/BBs is intimately linked to cytoskeletal networks (Boisvieux-Ulrich et al., 1990; Herawati et al., 2016; Lemullois et al., 1988; Werner et al., 2011). The organization of these networks evolves during MCC maturation, allowing first to direct BBs towards the apical surface and then to orient and space them. By using chemical cytoskeleton inhibitors, it has been possible to alter migration, orientation or dispersion of BBs, thus attributing specific functions to actin filaments and MTs (Boisvieux-Ulrich et al., 1990; Werner et al., 2011). Our data revealed that establishment of proper actin filamentous networks require the presence at BBs of both Lrrcc1 and Ccdc61. Our data, however, do not help to resolve how these proteins participate in actin network assembly. They could for instance be necessary for BBs to nucleate

actin filaments in a RhoA-dependent manner (Chevalier et al., 2015; Pan et al., 2007; Park et al., 2008). Alternatively, they could be involved in the formation, maintenance or activity of ciliary adhesions, which link BBs and rootlets with actin filaments (Antoniades et al., 2014). Future studies should address these and other possibilities to help elucidating the precise implication of Lrrcc1 and Ccdc61 in MCC actin network formation. In contrast to actin filaments and MTs, the contribution of IFs to the organization of MCCs remains unknown. Our analysis did not reveal the presence of IFs at the stage of centriole apical migration, ruling out their implication at this step. In mature MCCs, a prominent IF network adopts an annular shape around BBs, similar to the apical F-actin network, but which appears to form more basally, extending below the BB level, where rootlets are found (Fig. 4A' and 6B')(Sandoz et al., 1988). This IF network collapsed in MCCs deprived of Lrrcc1 and Ccdc61, suggesting that IFs could interact with the base of BBs and/or ciliary rootlets, through molecular complexes dependent on these two structural proteins. This first rudimentary analysis makes the *Xenopus* epidermis an attractive paradigm to address the specific role of IFs in MCC organization and function. In particular, it would be interesting to evaluate the possible link between actin and IF networks.

In contrast to the BF, which functions as an MT-organizing center (Clare et al., 2014; Kunimoto et al., 2012), the role of the rootlet appendage is less clear. Among proposed functions, it is generally believed to serve as an anchor, allowing BBs to maintain their position at the apical surface, and resist mechanical forces generated by ciliary beating (Antoniades et al., 2014; Bustamante-Marin et al., 2019; Yang et al., 2005; Yang and Li, 2005). In line with this, rootlets are scaffolds for molecular interactions, among which ciliary adhesion complexes were found to organize the short actin filaments that cross-link BBs together and help beating synchronization (Antoniades et al., 2014; Walentek et al., 2016; Werner et al., 2011). Here, we observed that Ccdc61, Pcnt and γ-Tubulin associate to rootlets in mature epidermal MCCs of *Xenopus.* Ccdc61 was recently shown to be a paralog of the scaffolding protein Sas6, known to

establish the 9-fold rotational symmetry of MTs during centriole duplication (Ochi et al., 2020). Interestingly, an evolutionary conserved interaction between Sas6 and Pcnt has recently been reported (Ito et al., 2019). Furthermore, Pcnt is known for its ability to recruit γ-Tubulin to assemble a macro-molecular complex allowing MT nucleation at the centrosome, and at mitotic spindles (Woodruff et al., 2014). Based on this information and our own observations, it is tempting to propose that Ccdc61 may help Pcnt recruitment/stabilization at the rootlet, which in turn would favour γ-Tubulin recruitment and MT nucleation. Alternatively, the reported interaction of Ccdc61 with MTs (Ochi et al., 2020) may be important to link pillar MTs emanating from the BF (Clare et al., 2014) with nearby rootlets, which could further strengthen the mechanical coupling between adjacent BBs, to optimize their coordinated orientation and synchronized beating. In support of this hypothesis, it is relevant to recall that Clamp/Spef1 is also a MT-binding factor (Dougherty et al., 2005; Kim et al., 2018; Werner et al., 2014). Future super-resolution and EM studies should investigate the possible link between MTs and rootlets. Unexpectedly, we found that cilia in Lrrcc1 and Ccdc61 morphant MCCs often beat very poorly. Proper ciliary beating entails correct axonemal structure and delivery of dynein motors to maintain ciliary motion (Huizar et al., 2018; Satir et al., 2014). Although we have not investigated these features, it is possible that the lack of Lrrcc1 and Ccdc61 compromises the capacity of rootlets to help trafficking towards the axoneme of essential structural or motor effectors (Gray et al., 2009; Mohan et al., 2013; Park et al., 2008; Yang and Li, 2005).

From the nanoscopic organization of organelles to the cellular function and physiology of the organism, all scales are coupled. The emergence of the locomotor function in planarians is a striking example of such coupling in multiciliated epithelia. In this model, polarization of BBs relies on their chiral construction, which mobilizes Lrrcc1 and Ccdc61. This polarization allows the establishment of bilateral symmetry of the ventral multiciliated epidermis, which in turns governs the orientation of the worm movement (Basquin et al., 2019). In addition, retro-control

loops exist between the different scales. For instance, in mouse ependymal MCCs, the establishment of a dense actin network that confers stability to BBs and cilia is dependent on active ciliary beating (Mahuzier et al., 2018). Thus, understanding such highly integrated systems implies analyzing multiple scales, as well as their coupling and feedback mechanisms. The present multi-scale study correlates the absence of structural proteins at BB appendages to MCC disorganization, defective flow production and impaired resistance to pathogens. Despite a wealth of studies on the *Xenopus* ciliated embryonic skin, it was unknown whether cilia-powered flow could limit infections by environmental pathogens. In that respect, the function of the *Xenopus* mucociliary epidermis is similar to that of the mucociliary epithelium that ensures the clearance of incoming pathogens in mammalian airways. In airways, cilia beating helps to propel a viscous layer of mucus trapping foreign particles, which lies on top of an aqueous periciliary layer. In contrast, in the *Xenopus* skin, the mucus layer is about 6 μm thick and sits right on top of the epithelium (Dubaissi et al., 2018), so that the 15 μm-long cilia actually beat in water to prevent attachment of micro-organisms. Thus, unlike in airways, the mucus on the frog embryonic skin may not be propelled as a coherent layer, which would explain the much lower density of MCCs necessary in this system. Although additional functions, such as oxygenation of the skin, are not ruled out, our proposed pathogen clearance function is consistent with the resorption of MCCs in pre-metamorphic tadpoles (Tasca et al., 2020), at a stage when innate immunity is in place (Robert and Ohta, 2009).

Materials and methods

Ethics statement

All experiments were performed following the Directive 2010/63/EU of the European parliament and of the council of 22 September 2010 on the protection of animals used for scientific purposes and approved by the "Direction départementale de la Protection des

Populations, Pôle Alimentation, Santé Animale, Environnement, des Bouches du Rhône " (agreement number F1305521).

RNA probes and whole mount *in situ* hybridization

cDNA fragments from *Xenopus laevis lrrcc1*.L (entrez gene 431936), and *ccdc61*.L (entrez gene 734655) were amplified from commercial cDNA (Horizon discovery) by PCR using the following primers:

lrrcc1 forward: 5'-GCGAACGGACACAGACAGTA-3';

lrrcc1 reverse: 5'-GAATTCCATGGTAGTCAGCTCCTGC-3';

ccdc61 forward: 5'-GCGGCCGCAAGTGGAGGATGCTGTGACC-3';

ccdc61 reverse: 5'-GAATTCACGGATGAACTGCGTCTCTG-3'.

PCR products were cloned in pBlueScript KS+ vector and digoxigenin-labelled probes were generated from linearized plasmids using RNA-labeling mix (Roche). Whole-mount chromogenic *in situ* hybridization was performed as described previously (Marchal 2009) using 40ng of Digoxygenin-labelled probe. Pictures were taken with the stereomicroscope Leica MZ125 coupled to NIKON digital Sight DS-Fi1 camera.

Plasmids, RNAs, and Morpholinos

To generate plasmids for RNA synthesis and micro-injection, the ORFs of *lrrcc1* and *ccdc61* were amplified by PCR using the following primers:

lrrcc1-forward: 5' TCTTTTTGCAGGATCACAATGGCAGGCACGGACCCACGAA 3';

lrrcc1-reverse: 5' CTTTACTCATTCTAGAAAATTCTTTTTGGATGTCACTTAG 3';

ccdc61-forward: 5' TCTTTTTGCAGGATCACAATGGAGGATACAGAGTTTGCT 3';

ccdc61-reverse: 5' CTTTACTCATTCTAGACTGCATCAGTAAGTACCCGCTGGCT 3'.

PCR products were subcloned in frame with GFP sequence in 3' into pCS2+-GFP vector using In-Fusion® HD Cloning Kit (Takara Bio USA, Inc.). For rescue experiments, silent mutations were introduced by PCR in the original Ccdc61 sequence (3' GAG-GAT-ACA-GAG-TTT-GCT-GAA-G 5') to generate a Ccdc61-GFP construct (named MOresCcdc61-GFP) with a sequence resistant to MO ATG (3' GA**A**-GA**C**-AC**G**-GA**A**-TT**C**-GCT-GAA 5'). pCS2+-mRFP was used to generate an injection reporter.

The cDNA fragment coding for amino-acids 3340 to 3643 of the full-length *Xenopus laevis* Pcnt was amplified by PCR from a partial cDNA clone (IMAGE 5156155, Source Bioscience). PCR products were cloned by Gateway® recombination into pGEX6P3 (GE Healthcare Life Sciences) and pEGFP-C1 (Clontech) to produce GST fusion proteins and express GFP-tagged proteins, respectively. The Centrin-RFP plasmid was a kind gift from JB Wallingford.

Capped mRNAs were synthetized from linearized vectors using the SP6 mMESSAGE mMACHINE® Kit (Ambion Life Technologies) and purified with the MEGAclear™ Kit (Ambion Life Technologies).

Two independent morpholino antisense oligonucleotides were designed against *lrrcc1* and *ccdc61* (GeneTools, LLC). *lrrcc1*-ATG-MO: 5' GTGCCTGCCATTCTCCCGCAACAAA 3'; *lrrcc1*-Spl-MO: 5' ACTGAAGCCATGCTGCTTACCTGGA 3'; *ccdc61*-ATG-MO: 5' CTTCAGCAAACTCTGTATCCTCCAT 3'; *ccdc61*-Spl-MO: 5' TGTCTCCCACTTCTACTCACATTGA 3'.

<u>*Xenopus* embryo injections</u>

Eggs obtained from wild-type *Xenopus laevis* females of 2 to 5 years of age (NASCO, USA) were fertilized *in vitro*, dejellied and cultured as described previously (Marchal et al., 2009). 20-30 ng of MO was injected (alone or with 200-500pg of mRFP tracer) in one or two animal-ventral blastomere (presumptive epidermis) at different stages depending on the experiment

(Table S2). Working amounts of MOs were first calibrated to optimize embryo survival. Validation of MOs efficacy in depleting the target protein was confirmed based on Lrrcc1 antibody and Ccdc61-GFP signal disappearance. For rescue experiments, a sequential injection strategy was adopted to obtain mosaic embryos containing differentially marked morphant and rescued MCCs. At 4-cell stage, *lrrcc1* and *ccdc61*-ATG-MOs + Centrin-RFP or *lrrcc1* and *ccdc61*-Spl-MOs + Centrin-RFP was injected At 16-cell stage, the same embryos were injected with Lrrcc1-GFP or MOresCcdc61-GFP mRNAs.

After injection, embryos were incubated at different temperatures between 13°, 18° and 23°C in MBS 0.1x until they reached the desired developmental stage. Whole-embryos were fixed in different conditions (Table S3) and stored in 100% methanol at -20°C in preparation for immunofluorescent staining.

Embryo deciliation

Stage 31 embryos were incubated for 2h in a 35-mm Petri dish containing 2 ml of dibucaine hydrochloride (200µM in MBS 0.1X; Fluka D0638-16). After a rapid wash in MBS 0.1x embryos were immediately fixed by incubation in MetOH 100% at -20°C for two days before being further processed for immunofluorescent staining.

Immunostaining

After a sequential re-hydration in solutions with decreasing methanol concentrations, embryos were incubated in blocking solution (3% Bovine Serum Albumin (BSA) in PBS 1x) for 1h at room temperature (RT) and subsequently in primary antibodies diluted in 3% BSA overnight at 4°C (Table S3). After washing in PBS 1x embryos were incubated with fluorescently labelled secondary antibodies diluted in 3% BSA for 1h at RT (Table S4). After washing, embryos were mounted in Mowiol (Sigma-Aldrich) between slide and coverslip.

Confocal Microscopy

Confocal pictures were acquired using ZEISS LSM 780 right standing AxioImager Z2 and ZEISS LSM 880 reverse standing AxioObserver 7 equipped with 20x and 63x oil objectives. Two- or three-colors confocal z-series images (z-slices interval between 0.3-0.8nm) were acquired using sequential laser excitation. When necessary, images were converted into single plane maximum intensity projection (MIP) and edited using Image J 2.0.0 software. ClearVolume Plugin for ImageJ (Royer et al., 2015) was used for 3D visualization of basal bodies.

Image analysis

F-actin and Pcnt signals were quantified by measuring the mean pixel intensity per MCC with ImageJ.

BB docking was quantified manually by counting the number of z-slices containing Centrin- or Centrin-RFP-positive centrioles along the apical-basal axis for each cell. These values were transformed in µm based on the interval size between slices set during confocal acquisition.

BB spacing analysis was performed from Centrin or Centrin-RFP immunostaining images using custom made Matlab scripts. After manual segmentation of individual cells, the script (i) automatically detects, and segment individual BBs within each cell. Only apically docked and isolated BBs are considered, omitting those located below the apical cell membrane or in dense clusters; (ii) determine the centroid of each BB; (iii) use XY coordinates of all the centroids to build triangles between the nearest neighbors with the Delaunay Triangulation Matlab script. Once the triangulation is obtained, areas of the triangles are measured in $pixel^2$ and transformed in μm^2 based on the pixel size of each acquisition.

BB orientation was analyzed using a home-made ImageJ script (designed by R. Flores-Flores). The script (i) automatically detects individual MCCs in the field of view; (ii) automatically detects individual BBs in each MCC; (iii) traces a vector from Centrin to γ-Tubulin spots (a threshold is applied for γ-Tubulin channel in order to detect only the BF associated spot, and not the rootlet spots) for each BB and calculate its angle with the vertical axis. The output of the script is a list of angles that were plotted using the Oriana software (Version 4.02, Kovach Computing Services) to obtain a graphical representation of their distribution in 25,7° bins, with 95% of confidence intervals. Finally, circular statistical analysis were performed (CSD, Rayleigh's Uniformity Test).

Transmission electron microscopy

Embryos were processed for electron microscopy as previously described (Revinski 2018) and cut transversely at midbody level (80 nm/slice) with a Leica Ultracut UC7 (Leica, Germany). Images were acquired using a Tecnai G2 (Thermofisher, USA) microscope equipped with a Veleta camera (Olympus, Japan).

Cell culture and Western Blot

Simian COS-1 cells were grown in DMEM supplemented with 10% heat inactivated FCS and transfected with Fugene HD (Roche Applied Science) according to manufacturer's protocol. Transfected or control cells were washed in PBS and lysed in 50 mM Tris HCl pH 7.5, 150 mM NaCl, 1 mM EDTA, containing 1% NP-40 and 0.25% sodium deoxycholate (modified RIPA) plus a Complete Protease Inhibitor Cocktail (Roche Applied Science) on ice. Cell extracts separated on polyacrylamide gels were transferred onto Optitran membrane (Whatman), followed by incubation with rabbit anti-GFP (1:5000, Abcam, ab290), or homemade rabbit anti-Pcnt antibody (1 µg/ml) produced by immunization with recombinant portion of *Xenopus laevis*

Pcnt (XP_018091513.1, residues 3340-3643), and horseradish peroxidase-conjugated secondary antibody (Jackson Immunoresearch Laboratories, 711-035-152). Signal obtained from enhanced chemiluminescence (Western Lightning ECL Pro, Perkin Elmer) was detected with MyECL Imager (ThermoFisher Scientific).

For MO validation by Western Blot, animal caps from control, Lrrcc1-GFP +/- MO, Ccdc61-GFP +/- MO, injected embryos were obtained by manual dissection from stage 10 (n= 50 embryos/condition) in 1X MBS and kept in 0,5X MBS until matched control embryos reached stage 25. Then they were immediately lysed in 200 µL of RIPA buffer (50mM Tris-HCl pH 7.5, 150 mM NaCl, 1% NP40, 0.1% SDS, 0,5% deoxycholate de sodium) containing protease inhibitors tablet (Pierce). Total protein concentration was determined by Bradford assay (Invitrogen) and samples were prepared in LDS sample buffer (Invitrogen) containing a reducing agent. Samples in LDS buffer were denatured 5 min at 100°C and 120 µg of proteins were loaded and separated on 4-20% SDS-PAGE (Mini-PROTEAN® TGX™ #456109, Biorad). Following migration, proteins were transferred onto 0,45 µm nitrocelullose membranes (GE Heathcare). Membranes were blocked in Tris-buffered saline, 1 hour at RT and then incubated overnight at 4°C with the primary antibody. After 3 washes in TBST buffer for 10 min, the membrane was incubated with the appropriate HRP conjugated secondary antibody (Jackson ImmunoResearch) diluted at 1/5000 in TBST-5% dry fat milk and signals were detected using chemiluminescence (See Table S4). Bands were then quantified by densitometry using Image J software and protein level expression was normalized with respect to the loading control protein.

Flow and cilia beating measurements

Stage 31 living embryos were placed in anaesthetic solution media (MS222 0.02% in MBS 0.1x) in a home-made 3D-printed Petri Dish specially designed to maintain them with the dorsal

side on the top. The setup was placed under compact Stereo Microscope ZEISS Stemi 305 coupled to ZEISS Axiocam 105 Color microscope camera. Timelapse recording was done after release of 1µl of visible dyed microspheres (Bangs Laboratories: DSCR006, Mean diameter 5.19 µm, diluted 1/2 in MBS 0,1x) at the anterior front of the embryo.

Cilia beating frequency was analyzed on the same pool of living embryos. Embryos were placed between a glass slide and a coverslip with a drop of anaesthesic medium (MBS 0.1x – MS222 0.02x) surrounded by grease (high vacuum grease DOW CORNING, Sigma-Aldrich Z273554-1EA) to stick the coverslip. Movies with a duration of 3 seconds (250 fps) were recorded at the ventral border of the embryos with a Nikon eclipse Ti-E microscope and a 63x long working distance air objective. Computation of cilia beat frequency (CBF) was done using an in-house routine developed in python (Khelloufi et al. 2018). The resulting frequencies (Hz) shown in the quantification represent the mean CBF computed over all visible cilia per individual MCC. Movies are played at 50fps to observe better the beating strokes and defaults. After flow and CBF recording, MO efficiency was assessed in those embryos by immunostaining for Centrin, Acetylated-α-tubulin and mRFP (injection tracer).

Embryo survival to *Aeromonas hydrophila*

Aeromonas hydrophila (Chester Stanier, ATCC®7966 kindly provided by E. Dubaissi) colonies were grown for 48h at 37°C on LB Agar + 30µg/mL Kanamycin. Next, individual colonies were cultured in 10mL LB + 30µg/mL Kanamycin overnight at 37°C. The OD_{600} (OD600 DiluPhotometer version1.4, Implen) was measured and the culture was either diluted in LB or grown further to reach an OD_{600} of 0.2. Cultures were centrifuged 10 min at 3500 xg and the bacteria pellet was resuspended in the same volume of MBS 0.1x. Controls (Non-injected or mRFP-injected) and morphant (Lrrcc1-MO+mRFP or Ccdc61-MO+mRFP)

embryos were incubated from St 31 during 72h at 13°C in 3mL of bacteria containing medium. Survival was assessed by recording active response to touch at 2h, 4h, 24h, 48h and 72h.

At the end of the experiment, MO efficiency was assessed by immunostaining for Centrin, Acetylated-α-tubulin and mRFP tracer.

Statistics

For all experiments, statistical analysis of significance was done using GraphPad Prism (version 8.2.0 for Windows, GraphPad Software, San Diego, California USA). First, the normality of data (Gaussian distribution) was tested using D'agostino & Pearson test (if n>50) or Shapiro-Wilk test (if n<50). When the data followed a normal distribution, we then compared them using parametric Student t-tests (between 2 groups) or one One-way ANOVA (between >2 groups). When data did not follow a normal distribution, we compared them using Mann-Whitney (2 groups) or Kruskal-Wallis (>2 groups) non-parametric tests. p = 0.0001 - 0.001 or <0.0001 was considered extremely significant (***), p = 0.001 - 0.01 was considered very significant (**); p = 0.01 - 0.05 was considered significant (*) and p = ≥0.05 was considered not significant (ns). Number of embryos and experiments performed for all analysis are listed in Table S5.

Acknowledgements

The authors wish to thank J. Azimzadeh, P. Walentek, E. Dubaissi and B. Mitchell for the gift of reagents. Imaging in IBDM was performed on PiCSL-FBI core facility, supported by the French National Research Agency through the program "Investments for the Future" (France-BioImaging, ANR-10-INBS-04). The authors thank Florian Roguet for *Xenopus* care, Rémi Flores-Flores for ImageJ macro development, Brice Detailleur for 3D printing of embryo

holders, Fabrice Richard, Nicolas Brouilly and Aicha Aouane from IBDM electron microscopy facility.

Authors contribution

AN performed and analyzed most experiments. CB, OR, EB, and LK analyzed experiments. OR generated and characterized Pcnt antibodies. VT performed and analyzed Pcnt immunostaining. CS performed Western Blot analyses. EB wrote scripts to analyze BB spacing. AV and EL designed, and EL performed and analyzed cilia beating experiments. AN and CB drafted the original manuscript. LK edited the manuscript. LK designed and supervised the study and obtained funding. All authors commented on the manuscript.

Competing interests

No competing interests.

Funding

This project was funded by grants from the Agence Nationale de la Recherche (Oricen, 15-CE13-0003-02) and the Fondation pour la Recherche Médicale (EQU201903007834). AN was supported by the French Ministry for Research, Superior Education and Innovation, and by the Fondation pour la Recherche Médicale.

References

Adams, G.M., Wright, R.L. and Jarvik, J.W. (1985). Defective temporal and spatial control of flagellar assembly in a mutant of *Chlamydomonas reinhardtii* with variable flagellar number. *J. Cell Biol.* **100**, 955-964.

Al Jord, A., Lemaitre, A.I., Delgehyr, N., Faucourt, M., Spassky, N. and Meunier, A. (2014). Centriole amplification by mother and daughter centrioles differs in multiciliated cells. *Nature.* **516**, 104-107.

Antoniades, I., Stylianou, P. and Skourides, P.A. (2014). Making the connection: ciliary adhesion complexes anchor basal bodies to the actin cytoskeleton. *Dev. Cell.* **28**, 70-80.

Barenz, F., Kschonsak, Y.T., Meyer, A., Jafarpour, A., Lorenz, H. and Hoffmann, I. (2018). Ccdc61 controls centrosomal localization of Cep170 and is required for spindle assembly and symmetry. *Mol. Biol. Cell.* **29**, 3105-3118.

Basquin, C., Ershov, D., Gaudin, N., Vu, H.T., Louis, B., Papon, J.F., Orfila, A.M., Mansour, S., Rink, J.C. and Azimzadeh, J. (2019). Emergence of a Bilaterally Symmetric Pattern from Chiral Components in the Planarian Epidermis. *Dev. Cell.* **51**, 516-525 e515.

Bengueddach, H., Lemullois, M., Aubusson-Fleury, A. and Koll, F. (2017). Basal body positioning and anchoring in the multiciliated cell *Paramecium tetraurelia*: roles of OFD1 and VFL3. *Cilia*. **6**, 6.

Boisvieux-Ulrich, E., Laine, M.C. and Sandoz, D. (1990). Cytochalasin D inhibits basal body migration and ciliary elongation in quail oviduct epithelium. *Cell Tissue Res.* **259**, 443-454.

Boon, M., Wallmeier, J., Ma, L., Loges, N.T., Jaspers, M., Olbrich, H., Dougherty, G.W., Raidt, J., Werner, C., Amirav, I. et al. (2014). MCIDAS mutations result in a mucociliary clearance disorder with reduced generation of multiple motile cilia. *Nat. Commun.* **5**, 4418.

Boutin, C. and Kodjabachian, L. (2019). Biology of multiciliated cells. *Curr. Opin. Genet. Dev.* **56**, 1-7.

Boutin, C., Labedan, P., Dimidschstein, J., Richard, F., Cremer, H., Andre, P., Yang, Y., Montcouquiol, M., Goffinet, A.M. and Tissir, F. (2014). A dual role for planar cell polarity genes in ciliated cells. *Proc. Natl. Acad. Sci. U S A.* **111**, E3129-3138.

Briggs, J.A., Weinreb, C., Wagner, D.E., Megason, S., Peshkin, L., Kirschner, M.W. and Klein, A.M. (2018). The dynamics of gene expression in vertebrate embryogenesis at single-cell resolution. *Science*. **360**.

Brooks, E.R. and Wallingford, J.B. (2014). Multiciliated cells. *Curr. Biol.* **24**, R973-982.

Bustamante-Marin, X.M., Yin, W.N., Sears, P.R., Werner, M.E., Brotslaw, E.J., Mitchell, B.J., Jania, C.M., Zeman, K.L., Rogers, T.D., Herring, L.E. et al. (2019). Lack of GAS2L2 Causes PCD by Impairing Cilia Orientation and Mucociliary Clearance. *Am. J. Hum. Genet.* **104**, 229-245.

Chevalier, B., Adamiok, A., Mercey, O., Revinski, D.R., Zaragosi, L.E., Pasini, A., Kodjabachian, L., Barbry, P. and Marcet, B. (2015). miR-34/449 control apical actin network formation during multiciliogenesis through small GTPase pathways. *Nat. Commun.* **6**, 8386.

Chien, Y.H., Keller, R., Kintner, C. and Shook, D.R. (2015). Mechanical strain determines the axis of planar polarity in ciliated epithelia. *Curr. Biol.* **25**, 2774-2784.

Chung, M.I., Kwon, T., Tu, F., Brooks, E.R., Gupta, R., Meyer, M., Baker, J.C., Marcotte, E.M. and Wallingford, J.B. (2014). Coordinated genomic control of ciliogenesis and cell movement by RFX2. *eLife*. **3**, e01439.

Chuyen, A., Rulquin, C., Daian, F., Thome, V., Clement, R., Kodjabachian, L. and Pasini, A. (2021). The Scf/Kit pathway implements self-organized epithelial patterning. *Dev. Cell.* **56**, 795-810 e797.

Clare, D.K., Magescas, J., Piolot, T., Dumoux, M., Vesque, C., Pichard, E., Dang, T., Duvauchelle, B., Poirier, F. and Delacour, D. (2014). Basal foot MTOC organizes pillar MTs required for coordination of beating cilia. *Nat. Commun.* **5**, 4888.

Collins, C., Kim, S.K., Ventrella, R., Carruzzo, H.M., Wortman, J.C., Han, H., Suva, E.E., Mitchell, J.W., Yu, C.C. and Mitchell, B.J. (2021). Tubulin acetylation promotes penetrative capacity of cells undergoing radial intercalation. *Cell Rep.* **36**, 109556.

Collins, C., Majekodunmi, A. and Mitchell, B. (2020). Centriole Number and the Accumulation of Microtubules Modulate the Timing of Apical Insertion during Radial Intercalation. *Curr. Biol.* **30**, 1958-1964 e1953.

Deblandre, G.A., Wettstein, D.A., Koyano-Nakagawa, N. and Kintner, C. (1999). A two-step mechanism generates the spacing pattern of the ciliated cells in the skin of *Xenopus* embryos. *Development*. **126**, 4715-4728.

Dougherty, G.W., Adler, H.J., Rzadzinska, A., Gimona, M., Tomita, Y., Lattig, M.C., Merritt, R.C., Jr. and Kachar, B. (2005). CLAMP, a novel microtubule-associated protein with EB-type calponin homology. *Cell. Motil. Cytoskeleton.* **62**, 141-156.

Dubaissi, E., Rousseau, K., Hughes, G.W., Ridley, C., Grencis, R.K., Roberts, I.S. and Thornton, D.J. (2018). Functional characterization of the mucus barrier on the *Xenopus tropicalis* skin surface. *Proc. Natl. Acad. Sci. U S A*. **115**, 726-731.

Epting, D., Slanchev, K., Boehlke, C., Hoff, S., Loges, N.T., Yasunaga, T., Indorf, L., Nestel, S., Lienkamp, S.S., Omran, H. et al. (2015). The Rac1 regulator ELMO controls basal body migration and docking in multiciliated cells through interaction with Ezrin. *Development*. **142**, 1553.

Gaudin, N., Martin Gil, P., Boumendjel, M., Ershov, D., Pioche-Durieu, C., Bouix, M., Delobelle, Q., Maniscalco, L., Thanh Bich Ngan Phan., Heyer, V. et al. Evolutionary conservation of centriole rotational asymmetry in the human centrosome. *bioRxiv*, doi:10.1101/2021.07.21.453218.

Gray, R.S., Abitua, P.B., Wlodarczyk, B.J., Szabo-Rogers, H.L., Blanchard, O., Lee, I., Weiss, G.S., Liu, K.J., Marcotte, E.M., Wallingford, J.B. et al. (2009). The planar cell polarity effector Fuz is essential for targeted membrane trafficking, ciliogenesis and mouse embryonic development. *Nat. Cell Biol.* **11**, 1225-1232.

Guirao, B., Meunier, A., Mortaud, S., Aguilar, A., Corsi, J.M., Strehl, L., Hirota, Y., Desoeuvre, A., Boutin, C., Han, Y.G. et al. (2010). Coupling between hydrodynamic forces and planar cell polarity orients mammalian motile cilia. *Nat. Cell Biol.* **12**, 341-350.

Hagiwara, H., Kano, A., Aoki, T., Ohwada, N. and Takata, K. (2000). Localization of gamma-tubulin to the basal foot associated with the basal body extending a cilium. *Histochem. J.* **32**, 669-671.

Hein, M.Y., Hubner, N.C., Poser, I., Cox, J., Nagaraj, N., Toyoda, Y., Gak, I.A., Weisswange, I., Mansfeld, J., Buchholz, F. et al. (2015). A human interactome in three quantitative dimensions organized by stoichiometries and abundances. *Cell*. **163**, 712-723.

Herawati, E., Taniguchi, D., Kanoh, H., Tateishi, K., Ishihara, S. and Tsukita, S. (2016). Multiciliated cell basal bodies align in stereotypical patterns coordinated by the apical cytoskeleton. *J. Cell Biol.* **214**, 571-586.

Hoops, H.J., Wright, R.L., Jarvik, J.W. and Witman, G.B. (1984). Flagellar waveform and rotational orientation in a Chlamydomonas mutant lacking normal striated fibers. *J. Cell Biol*. **98**, 818-824.

Huizar, R.L., Lee, C., Boulgakov, A.A., Horani, A., Tu, F., Marcotte, E.M., Brody, S.L. and Wallingford, J.B. (2018). A liquid-like organelle at the root of motile ciliopathy. *eLife*. **7**.

Ito, D., Zitouni, S., Jana, S.C., Duarte, P., Surkont, J., Carvalho-Santos, Z., Pereira-Leal, J.B., Ferreira, M.G. and Bettencourt-Dias, M. (2019). Pericentrin-mediated SAS-6 recruitment promotes centriole assembly. *eLife*. **8**.

Kemp, A. (1996). Role of epidermal cilia in development of the Australian lungfish, *Neoceratodus forsteri (Osteichthyes*: *Dipnoi*). *J. Morphol.* **228**, 203-221.

Kim, S.K., Zhang, S., Werner, M.E., Brotslaw, E.J., Mitchell, J.W., Altabbaa, M.M. and Mitchell, B.J. (2018). CLAMP/Spef1 regulates planar cell polarity signaling and asymmetric microtubule accumulation in the *Xenopus* ciliated epithelia. *J. Cell Biol*. **217**, 1633-1641.

Klos Dehring, D.A., Vladar, E.K., Werner, M.E., Mitchell, J.W., Hwang, P. and Mitchell, B.J. (2013). Deuterosome-mediated centriole biogenesis. *Dev. Cell*. **27**, 103-112.

Kulkarni, S., Marquez, J., Date, P., Ventrella, R., Mitchell, B.J. and Khokha, M.K. (2021). Mechanical stretch scales centriole number to apical area via Piezo1 in multiciliated cells. *eLife*. **10**.

Kulkarni, S.S., Griffin, J.N., Date, P.P., Liem, K.F., Jr. and Khokha, M.K. (2018). WDR5 Stabilizes Actin Architecture to Promote Multiciliated Cell Formation. *Dev. Cell*. **46**, 595-610 e593.

Kunimoto, K., Yamazaki, Y., Nishida, T., Shinohara, K., Ishikawa, H., Hasegawa, T., Okanoue, T., Hamada, H., Noda, T., Tamura, A. et al. (2012). Coordinated ciliary beating requires Odf2-mediated polarization of basal bodies via basal feet. *Cell*. **148**, 189-200.

Lemullois, M., Boisvieux-Ulrich, E., Laine, M.C., Chailley, B. and Sandoz, D. (1988). Development and functions of the cytoskeleton during ciliogenesis in metazoa. *Biol. Cell*. **63**, 195-208.

Ma, L., Quigley, I., Omran, H. and Kintner, C. (2014). Multicilin drives centriole biogenesis via E2f proteins. *Genes Dev*. **28**, 1461-1471.

Mahuzier, A., Shihavuddin, A., Fournier, C., Lansade, P., Faucourt, M., Menezes, N., Meunier, A., Garfa-Traore, M., Carlier, M.F., Voituriez, R. et al. (2018). Ependymal cilia beating induces an actin network to protect centrioles against shear stress. *Nat. Commun*. **9**, 2279.

Meunier, A. and Azimzadeh, J. (2016). Multiciliated Cells in Animals. *Cold Spring Harb. Perspect. Biol*. **8**.

Mitchell, B., Jacobs, R., Li, J., Chien, S. and Kintner, C. (2007). A positive feedback mechanism governs the polarity and motion of motile cilia. *Nature*. **447**, 97-101.

Mitchell, B., Stubbs, J.L., Huisman, F., Taborek, P., Yu, C. and Kintner, C. (2009). The PCP pathway instructs the planar orientation of ciliated cells in the *Xenopus* larval skin. *Curr. Biol.* **19**, 924-929.

Miyatake, K., Kusakabe, M., Takahashi, C. and Nishida, E. (2015). ERK7 regulates ciliogenesis by phosphorylating the actin regulator CapZIP in cooperation with Dishevelled. *Nat. Commun*. **6**, 6666.

Mohan, S., Timbers, T.A., Kennedy, J., Blacque, O.E. and Leroux, M.R. (2013). Striated rootlet and nonfilamentous forms of rootletin maintain ciliary function. *Curr. Biol*. **23**, 2016-2022.

Muto, Y., Yoshioka, T., Kimura, M., Matsunami, M., Saya, H. and Okano, Y. (2008). An evolutionarily conserved leucine-rich repeat protein CLERC is a centrosomal protein required for spindle pole integrity. *Cell Cycle*. **7**, 2738-2748.

Nokhbatolfoghahai, M., Downie, J.R. and Ogilvy, V. (2006). Surface ciliation of anuran amphibian larvae: persistence to late stages in some species but not others. *J. Morphol*. **267**, 1248-1256.

Ochi, T., Quarantotti, V., Lin, H., Jullien, J., Rosa, E.S.I., Boselli, F., Barnabas, D.D., Johnson, C.M., McLaughlin, S.H., Freund, S.M.V. et al. (2020). CCDC61/VFL3 Is a Paralog of SAS6 and Promotes Ciliary Functions. *Structure*. **28**, 674-689 e611.

Pan, J., You, Y., Huang, T. and Brody, S.L. (2007). RhoA-mediated apical actin enrichment is required for ciliogenesis and promoted by Foxj1. *J. Cell Sci*. **120**, 1868-1876.

Park, T.J., Haigo, S.L. and Wallingford, J.B. (2006). Ciliogenesis defects in embryos lacking inturned or fuzzy function are associated with failure of planar cell polarity and Hedgehog signaling. *Nat. Genet*. **38**, 303-311.

Park, T.J., Mitchell, B.J., Abitua, P.B., Kintner, C. and Wallingford, J.B. (2008). Dishevelled controls apical docking and planar polarization of basal bodies in ciliated epithelial cells. *Nat. Genet.* **40**, 871-879.

Pizon, V., Gaudin, N., Poteau, M., Cifuentes-Diaz, C., Demdou, R., Heyer, V., Reina San Martin, B. and Azimzadeh, J. (2020). hVFL3/CCDC61 is a component of mother centriole subdistal appendages required for centrosome cohesion and positioning. *Biol. Cell*. **112**, 22-37.

Revinski, D.R., Zaragosi, L.E., Boutin, C., Ruiz-Garcia, S., Deprez, M., Thome, V., Rosnet, O., Gay, A.S., Mercey, O., Paquet, A. et al. (2018). CDC20B is required for deuterosome-mediated centriole production in multiciliated cells. *Nat. Commun*. **9**, 4668.

Robert, J. and Ohta, Y. (2009). Comparative and developmental study of the immune system in *Xenopus*. *Dev. Dyn*. **238**, 1249-1270.

Royer, L.A., Weigert, M., Gunther, U., Maghelli, N., Jug, F., Sbalzarini, I.F. and Myers, E.W. (2015). ClearVolume: open-source live 3D visualization for light-sheet microscopy. *Nat. Methods*. **12**, 480-481.

Sandoz, D., Chailley, B., Boisvieux-Ulrich, E., Lemullois, M., Laine, M.C. and Bautista-Harris, G. (1988). Organization and functions of cytoskeleton in metazoan ciliated cells. *Biol. Cell*. **63**, 183-193.

Satir, P., Heuser, T. and Sale, W.S. (2014). A Structural Basis for How Motile Cilia Beat. *Bioscience*. **64**, 1073-1083.

Sedzinski, J., Hannezo, E., Tu, F., Biro, M. and Wallingford, J.B. (2016). Emergence of an Apical Epithelial Cell Surface *In Vivo*. *Dev. Cell*. **36**, 24-35.

Silflow, C.D., LaVoie, M., Tam, L.W., Tousey, S., Sanders, M., Wu, W., Borodovsky, M. and Lefebvre, P.A. (2001). The Vfl1 Protein in *Chlamydomonas* localizes in a rotationally asymmetric pattern at the distal ends of the basal bodies. *J. Cell Biol*. **153**, 63-74.

Spassky, N. and Meunier, A. (2017). The development and functions of multiciliated epithelia. *Nat. Rev. Mol. Cell Biol*. **18**, 423-436.

Stubbs, J.L., Davidson, L., Keller, R. and Kintner, C. (2006). Radial intercalation of ciliated cells during *Xenopus* skin development. *Development*. **133**, 2507-2515.

Tasca, A., Helmstadter, M., Brislinger, M.M., Haas, M., Mitchell, B. and Walentek, P. (2020). Notch signaling induces either apoptosis or cell fate change in multiciliated cells during mucociliary tissue remodeling. *Dev. Cell*. **56**, 525-539.

Tateishi, K., Nishida, T., Inoue, K. and Tsukita, S. (2017). Three-dimensional Organization of Layered Apical Cytoskeletal Networks Associated with Mouse Airway Tissue Development. *Sci. Rep*. **7**, 43783.

Turk, E., Wills, A.A., Kwon, T., Sedzinski, J., Wallingford, J.B. and Stearns, T. (2015). Zeta-Tubulin Is a Member of a Conserved Tubulin Module and Is a Component of the Centriolar Basal Foot in Multiciliated Cells. *Curr. Biol*. **25**, 2177-2183.

Walentek, P., Boutin, C. and Kodjabachian, L. (2017). Planar cell polarity in ciliated epithelia. In *Cell Polarity in Development and Disease* (ed. D. Houston). Elsevier.

Walentek, P., Quigley, I.K., Sun, D.I., Sajjan, U.K., Kintner, C. and Harland, R.M. (2016). Ciliary transcription factors and miRNAs precisely regulate Cp110 levels required for ciliary adhesions and ciliogenesis. *eLife*. **5**.

Wallmeier, J., Al-Mutairi, D.A., Chen, C.T., Loges, N.T., Pennekamp, P., Menchen, T., Ma, L., Shamseldin, H.E., Olbrich, H., Dougherty, G.W. et al. (2014). Mutations in CCNO result in congenital mucociliary clearance disorder with reduced generation of multiple motile cilia. *Nat. Genet*. **46**, 646-651.

Werner, M.E., Hwang, P., Huisman, F., Taborek, P., Yu, C.C. and Mitchell, B.J. (2011). Actin and microtubules drive differential aspects of planar cell polarity in multiciliated cells. *J. Cell Biol*. **195**, 19-26.

Werner, M.E., Mitchell, J.W., Putzbach, W., Bacon, E., Kim, S.K. and Mitchell, B.J. (2014). Radial intercalation is regulated by the Par complex and the microtubule-stabilizing protein CLAMP/Spef1. *J. Cell Biol*. **206**, 367-376.

Woodruff, J.B., Wueseke, O. and Hyman, A.A. (2014). Pericentriolar material structure and dynamics. *Philos. Trans. R. Soc. Lond. B. Biol. Sci*. **369**.

Wright, R.L., Chojnacki, B. and Jarvik, J.W. (1983). Abnormal basal-body number, location, and orientation in a striated fiber-defective mutant of *Chlamydomonas reinhardtii*. *J. Cell Biol.* **96**, 1697-1707.

Yang, J., Gao, J., Adamian, M., Wen, X.H., Pawlyk, B., Zhang, L., Sanderson, M.J., Zuo, J., Makino, C.L. and Li, T. (2005). The ciliary rootlet maintains long-term stability of sensory cilia. *Mol. Cell. Biol*. **25**, 4129-4137.

Yang, J. and Li, T. (2005). The ciliary rootlet interacts with kinesin light chains and may provide a scaffold for kinesin-1 vesicular cargos. *Exp. Cell Res*. **309**, 379-389.

Yasunaga, T., Hoff, S., Schell, C., Helmstadter, M., Kretz, O., Kuechlin, S., Yakulov, T.A., Engel, C., Muller, B., Bensch, R. et al. (2015). The polarity protein Inturned links NPHP4 to Daam1 to control the subapical actin network in multiciliated cells. *J. Cell Biol*. **211**, 963-973.

Zhang, S. and Mitchell, B.J. (2015). Basal bodies in *Xenopus*. *Cilia*. **5**, 2.

Zhao, H., Zhu, L., Zhu, Y., Cao, J., Li, S., Huang, Q., Xu, T., Huang, X., Yan, X. and Zhu, X. (2013). The Cep63 paralogue Deup1 enables massive de novo centriole biogenesis for vertebrate multiciliogenesis. *Nat. Cell Biol*. **15**, 1434-1444.

Figure legends

Figure 1. Lrrcc1 and Ccdc61 associate with centrioles in multiciliated cells.

(A,B) MIPs (maximum intensity projections) of confocal acquisitions of MCCs stained with Lrrcc1 (green) and Centrin (red) antibodies at St18 (A) or St31 (B). (C) MIP of confocal acquisitions showing the localization of Lrrcc1 (green) compared to Centrin (red) and γ-Tubulin (white). (D) MIP of confocal acquisitions showing the localization of Lrrcc1 (red) compared to Clamp-GFP (green) and Centrin (white). White arrows indicate the BBs analyzed in 3D with ClearVolume in E and F. (E,F) ClearVolume 3D top and lateral views of single BBs from C and D. (G,H) MIPs of confocal acquisitions from MCCs stained with Ccdc61 (green) and Centrin (red) antibodies. (I) MIP of confocal acquisitions showing the localization of Ccdc61 (green) compared to Centrin (red) and γ-Tubulin (white). (J) MIP of confocal acquisitions showing the localization of Ccdc61 (red) compared to Clamp-GFP (green) and Centrin (white). White arrows indicate the BBs analyzed in 3D with ClearVolume in K and L. (K,L) ClearVolume 3D top and lateral views of single BBs from I and J. In A,B,G and H, white dashed boxes indicate higher magnification views presented below and the dashed white line sets the position of the lateral view.

Figure 2. Lrrcc1 and Ccdc61 are necessary for BB docking, spacing and orientation.

(A) MIPs of confocal acquisitions of MCCs from St 31 control, Lrrcc1 or Ccdc61 morphant embryos stained with Centrin antibody, or expressing Centrin-RFP, which was co-injected with MOs. (B) Graph displaying the apico-basal (A-B) distribution of centrioles within control, Lrrcc1 and Ccdc61 morphant and rescued (+mRNA) MCCs. Each point represents the maximum depth at which centrioles have been observed in each MCC. Horizontal lines represent the mean and SD (number of MCCs analyzed: control=28, *lrrcc1* ATG-MO with/without mRNA=36/41, *ccdc61* ATG-MO with/without mRNA=34/35, from 3 independent experiments). (C) MIPs of confocal acquisitions of apical BBs in MCCs from St 31 control, Lrrcc1 or Ccdc61 morphant embryos stained with Centrin antibody, or expressing Centrin-RFP, which was co-injected with MOs. The corresponding Delaunay triangulation outputs (see methods) are presented on the bottom row. Each colour is associated to a range of triangle areas in pixel^2. (D) Violin plots displaying the distribution of triangle areas in μm^2 of control, morphant and rescued MCCs. The horizontal line indicates the median, dashed lines indicate the quartiles (number

of MCCs analyzed: control=19, *lrrcc1* ATG-MO with/without mRNA=20/43, *ccdc61* ATG-MO with/without mRNA=27/28, from 3 independent experiments). (E) MIPs of confocal acquisitions of control and morphant MCCs stained with Centrin (red, centrioles) and γ-Tubulin (white, BF). At the right corner of each MIP, magnifications of the same MCCs are shown to better appreciate BB orientation. Below each cell, its respective rose histogram representing the distribution of BB orientations. The black line running from the centre of the diagram to the outer edge is the mean angle and the arcs extending to either side represent the confidence limits of the mean fixed at 95% (when the mean angle is only theoretical but not significant, the line turns pink). (F) Circular Standard Deviations of control, morphant and rescued MCCs. Each point represents a single cell. Horizontal lines represent the mean and SD (number of MCCs analyzed: control=125, *lrrcc1* ATG-MO with/without mRNA=24/40, *ccdc61* ATG-MO with/without mRNA=33/39, from 3 independent experiments). (G) Graph displaying the percentage of non-polarized MCCs (no significant mean angle of BBs within a cell can be calculated) following the Rayleigh statistical test (number of MCCs analyzed: control=591, *lrrcc1* ATG-MO=181, *ccdc61* ATG-MO=158, from 3 independent experiments). All confocal images are at the scale shown in (A). When the data followed a normal distribution, we compared them with One-way ANOVA, and if not, with Kruskal-Wallis test. For all graphs $p = 0.0001 - 0.001$ or <0.0001 (***), $p = 0.001 - 0.01$ (**); $p = 0.01 - 0.05$ (*) and $p \geq 0.05$ not significant (ns).

Figure 3. Ccdc61 is required for Pericentrin association to rootlet appendages.

(A) Transversal TEM acquisitions of BBs from St 31 control and morphant MCCs. Both fan-shape (blue arrow) and long (red arrow) rootlets could be observed in all conditions, but rarely on the same section. (B) Quantification of BB docking on TEM acquisitions to corroborate morpholino efficiency (number of BBs analyzed: control=134, *lrrcc1* ATG-MO=174, *ccdc61* ATG-MO=120, from 2 independent experiments). (C) Graph displaying the proportion of BBs with at least one (fan-shaped or long) or without rootlets quantified on TEM acquisitions. Please note that about 20% control BBs appear to lack rootlets due to the angle of the section. The same proportion was observed in Lrrcc1 and Ccdc61 morphant MCCs. Both docked and undocked BBs were scored. (D) MIPs of confocal acquisitions of MCCs stained with Pcnt (green), Centrin (red) and γ-Tubulin (white). The white arrow indicates the BB

analyzed in 3D in D'. (D') ClearVolume 3D top views of the BB pointed in D. (E) MIPs of confocal acquisitions of MCCs stained with Pcnt (red), and Clamp-GFP (green). The white arrow indicates the BB analyzed in 3D in E'. (E') ClearVolume 3D top view of the BB pointed in E. (F) MIPs of confocal acquisitions of St 31 Lrrcc1 and Ccdc61 morphant MCCs expressing Centrin-RFP (red) and stained with Pcnt antibody (green). White dashed boxes indicate high magnification views displayed on the right. (G) Quantification of Pcnt mean signal intensity. Each point represents an MCC. Horizontal lines represent the mean and SD (number of MCCs analyzed: control for Lrrcc1/Ccdc61=91/46, *lrrcc1* ATG-MO=136, *ccdc61* ATG-MO=143, from 3 independent experiments). When the data followed a normal distribution, we compared them with Student t-test, and if not, with Mann-Whitney test ($p = 0.0001$ - 0.001 or <0.0001 (***), $p \geq 0.05$ not significant (ns)).

Figure 4. Depletion of Lrrcc1 and Ccdc61 impairs apical and subapical actin networks in MCCs. (A-C) MIPs of confocal acquisitions of St31 control and morphant MCCs stained for F-actin (white, Sir-actin), Centrin (red, Ab in control, Centrin-RFP co-injected with MOs in morphants). Dashed boxes indicate high magnification views in A'-C'. (A'-C') Single slices of confocal acquisitions showing the apical or subapical (0.6 µm below) actin network in control and morphant cells. The dashed white line sets the position of the corresponding lateral view (bottom row). (D-E) Graph displaying the quantification of mean F-actin signal intensity in control and morphant MCCs. Horizontal lines represent the mean and SD (number of MCCs analyzed: control for Lrrcc1/Ccdc61=72/43, *lrrcc1* ATG-MO=31, ccdc61 Spl-MO=32, from 2 independent experiments). When the data followed a normal distribution, we compared them with Student t-test, and if not, with Mann-Whitney test ($p = 0.0001$ - 0.001 or <0.0001 (***), $p = 0.001$ - 0.01 (**); $p = 0.01$ - 0.05 (*) and $p = \geq 0.05$ not significant (ns)).

Figure 5. Depletion of Lrrcc1 and Ccdc61 causes apical MT network disorganization in MCCs. (A-E) MIPs of confocal acquisitions of St 31 control and morphant MCCs after deciliation stained with α-Tubulin (green, MTs) and Centrin antibody or expressing Centrin-RFP co-injected with MOs (red, BBs). All confocal images are at the scale shown in A. White dashed boxes indicate the high magnification views in A'-E'. (A', C', E') Apical confocal slices in control (A'), Lrrcc1 (C') and Ccdc61

(E') morphant cells. The regular MT network that links BBs in control cells appear irregular in morphant conditions. (B', D') MIPs of confocal acquisitions showing intense α-Tubulin signal around clustered BBs in Lrrcc1 and Ccdc61 morphant MCCs. Dashed white lines set the position of the corresponding lateral views shown on the bottom row. All magnifications are at the scale shown in A'.

Figure 6. Depletion of Lrrcc1 and Ccdc61 impairs apical intermediate filament network in MCCs.
(A-D) MIPs of confocal acquisitions of St 18 control MCC (A) and St 31 control (B) or morphant (C-D) MCCs stained for IFs (C-11 Ab, green) and BBs (Centrin Ab or Centrin-RFP co-injected with MOs, red). Dashed boxes indicate high magnification views in B'-D'. (B'-D') High magnification views of the zones boxed in B-D. The regular IF network that surrounds BBs in control cells appear much less dense in morphant conditions. White dashed lines set the position of the corresponding lateral views shown on the bottom row**.**

Figure 7. Lrrcc1 and Ccdc61 depletion impairs ciliary beating, flow production and embryo resistance against pathogens.
(A) Quantification of cilia beating frequency (Hz) in control and morphant MCCs. Each dot represents the mean ciliary beat frequency computed over all visible cilia per individual MCC . Horizontal lines represent the mean and SD (number of MCCs analyzed: control=13, *lrrcc1* ATG-MO=49, *ccdc61* ATG-MO=47, from 2 independent experiments). When the data followed a normal distribution, we compared them with Student t-test, and if not, with Mann-Whitney test (p = 0.0001 - 0.001 or <0.0001 (***)). (B) Still frames at 4 time-points taken from movie 3 showing the progression of the red dye along the flanks of control, Lrrcc1 and Ccdc61 morphant tadpoles. The black arrow on the top represents the flow along the anterior-posterior axis (A-P). (C) Percentage of the embryo length reached by the dye front in 12 seconds. Each bar represents one recorded embryo. Cases marked with an asterisk are those shown in B (number of embryos analyzed: control=12, *lrrcc1* ATG-MO=10, *ccdc61* ATG-MO=8). (D) Quantification of control and morphant tadpoles survival in presence or not of *A. hydrophila* bacteria (number of embryos analyzed: control without/with bacteria=73/84, GFP without/with bacteria=73/74,

lrrcc1 ATG-MO without/with bacteria=45/53, *ccdc61* ATG-MO without/with bacteria=35/38, from 3 independent experiments).

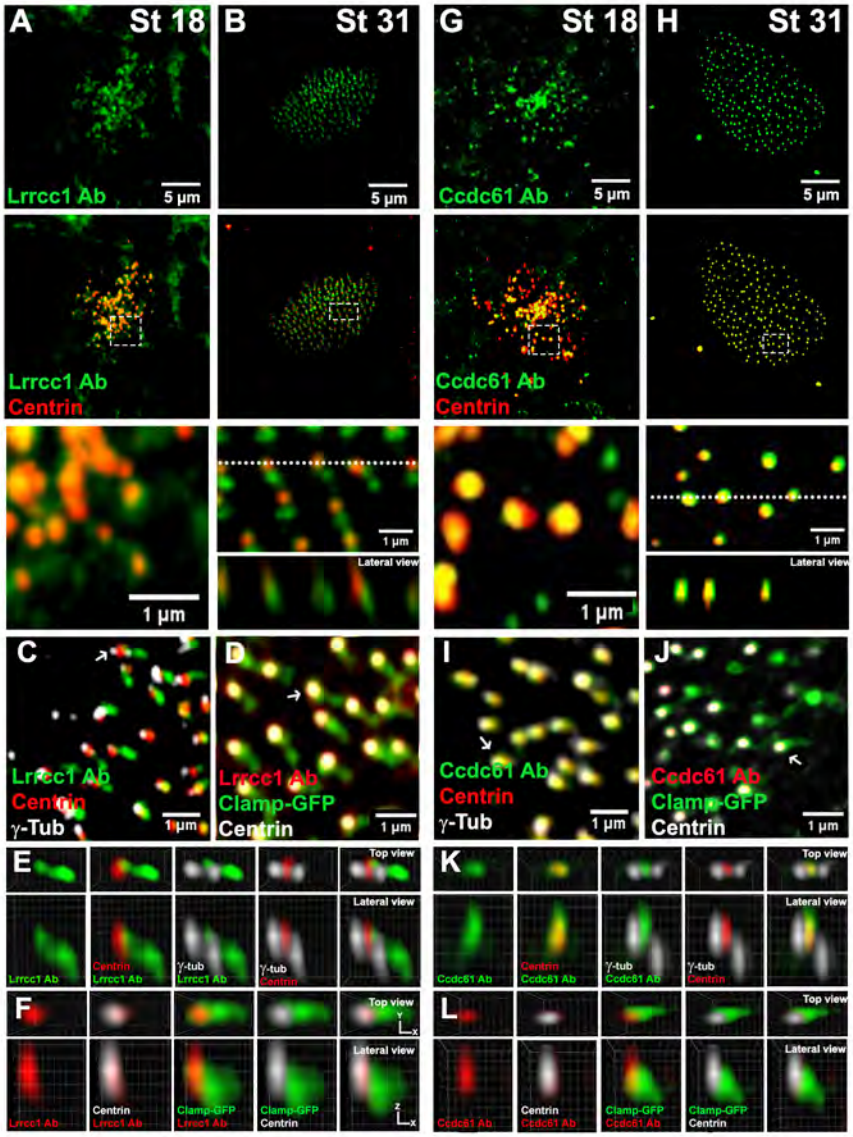
A
St 18
Lrrcc1 Ab
5 µm
B
St 31
5 µm
G
St 18
Ccdc61 Ab
5 µm
H
St 31
5 µm
Lrrcc1 Ab
Centrin
Ccdc61 Ab
Centrin
1 µm
Lateral view
C
Lrrcc1 Ab
Centrin
γ-Tub
D
Lrrcc1 Ab
Clamp-GFP
Centrin
I
Ccdc61 Ab
Centrin
γ-Tub
J
Ccdc61 Ab
Clamp-GFP
Centrin
E
F
K
L
Top view
Lateral view
Centrin
γ-tub
Clamp-GFP

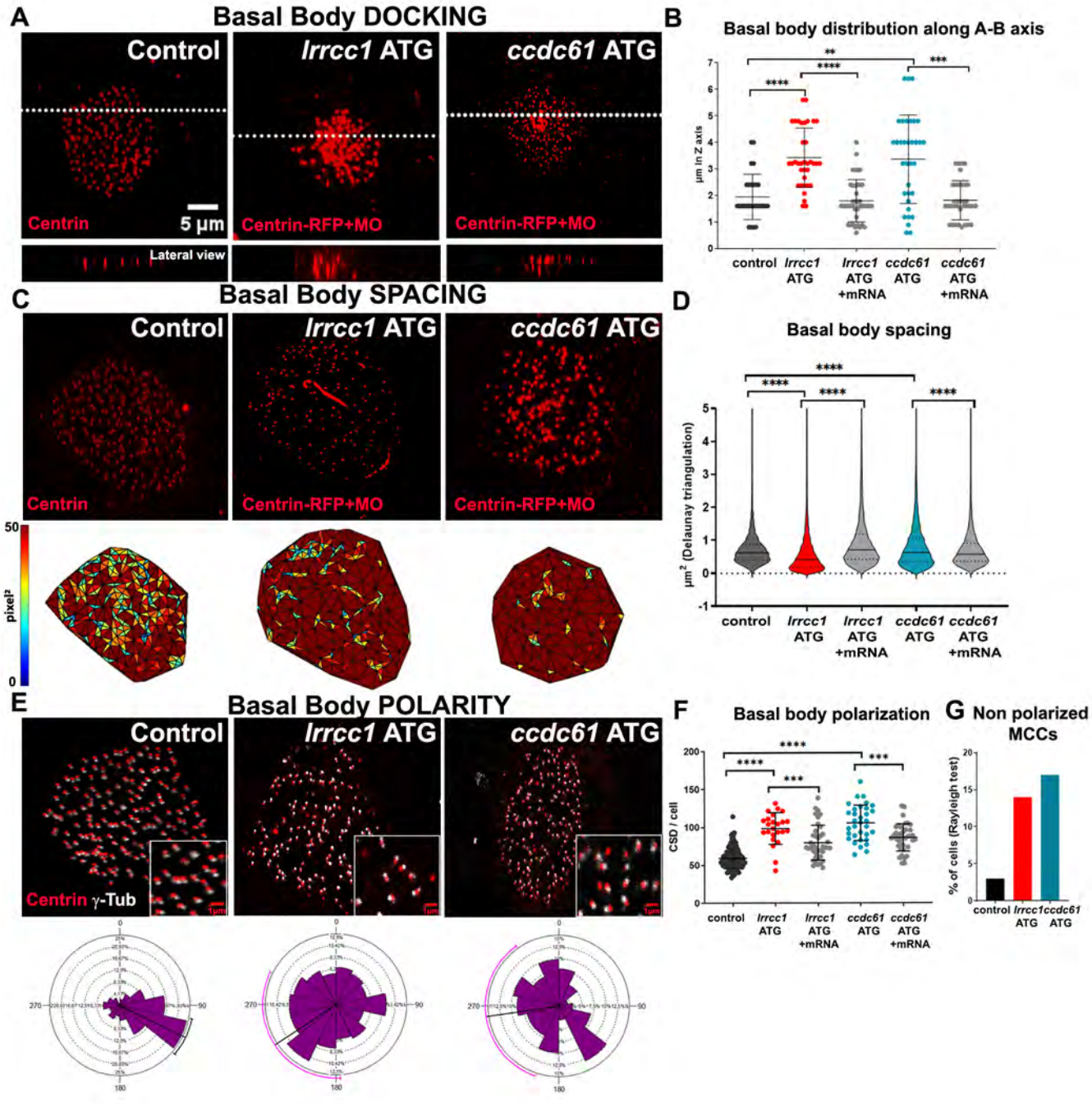
A
Basal Body DOCKING
Control
lrrcc1 ATG
ccdc61 ATG
Centrin
5 µm
Centrin-RFP+MO
Centrin-RFP+MO
Lateral view
B
Basal body distribution along A-B axis
µm in Z axis
control
lrrcc1 ATG
lrrcc1 ATG +mRNA
ccdc61 ATG
ccdc61 ATG +mRNA
C
Basal Body SPACING
Control
lrrcc1 ATG
ccdc61 ATG
Centrin
Centrin-RFP+MO
Centrin-RFP+MO
pixel²
50
0
D
Basal body spacing
µm² (Delaunay triangulation)
E
Basal Body POLARITY
Control
lrrcc1 ATG
ccdc61 ATG
Centrin γ-Tub
F
Basal body polarization
CSD / cell
G
Non polarized MCCs
% of cells (Rayleigh test)

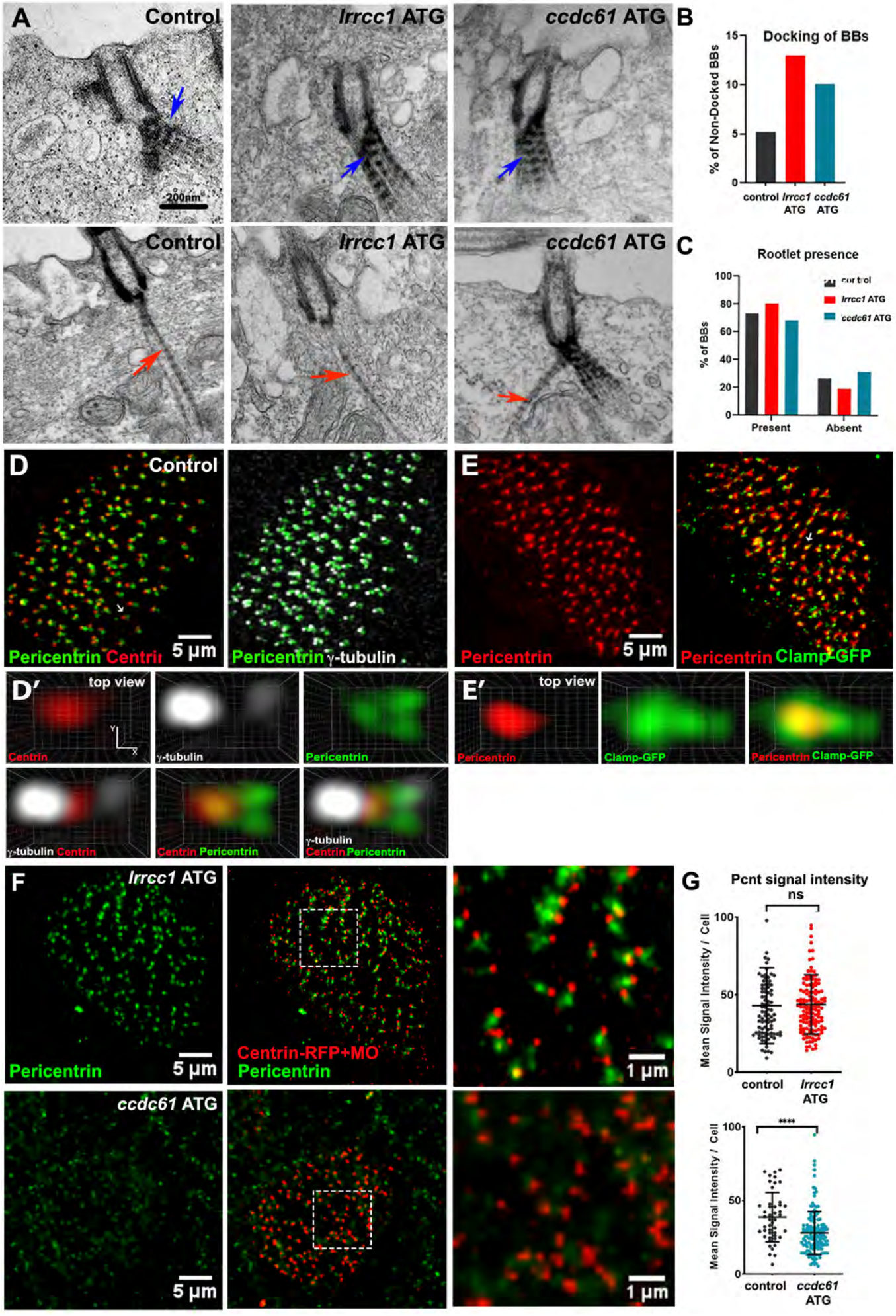
A
Control
lrrcc1 ATG
ccdc61 ATG
200nm
B
Docking of BBs
% of Non-Docked BBs
15
10
5
0
control
lrrcc1 ATG
ccdc61 ATG
C
Rootlet presence
% of BBs
100
80
60
40
20
0
control
lrrcc1 ATG
ccdc61 ATG
Present
Absent
D
Control
5 µm
Pericentrin Centrin
Pericentrin γ-tubulin
E
Pericentrin
5 µm
Pericentrin Clamp-GFP
D′
top view
Centrin
γ-tubulin
Pericentrin
γ-tubulin Centrin
Centrin Pericentrin
γ-tubulin Centrin Pericentrin
E′
top view
Pericentrin
Clamp-GFP
Pericentrin Clamp-GFP
F
lrrcc1 ATG
5 µm
Pericentrin
Centrin-RFP+MO
Pericentrin
1 µm
ccdc61 ATG
5 µm
1 µm
G
Pcnt signal intensity
ns
Mean Signal Intensity / Cell
100
50
0
control
lrrcc1 ATG
***
Mean Signal Intensity / Cell
100
50
0
control
ccdc61 ATG

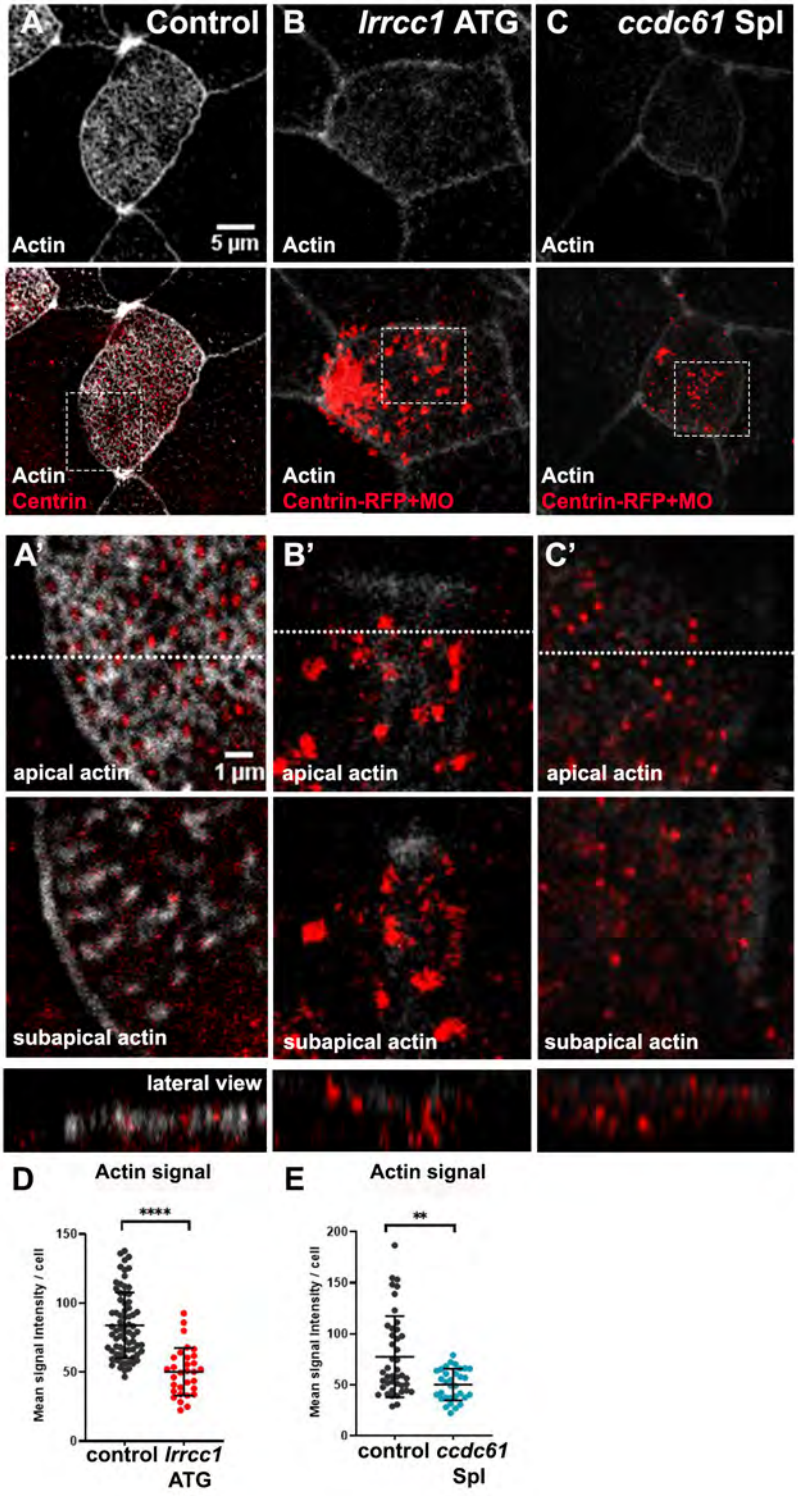
A Control
B lrrcc1 ATG
C ccdc61 Spl
Actin
5 µm
Actin
Actin
Actin
Centrin
Actin
Centrin-RFP+MO
Actin
Centrin-RFP+MO
A'
B'
C'
apical actin
1 µm
apical actin
apical actin
subapical actin
subapical actin
subapical actin
lateral view
D
Actin signal
****
Mean signal intensity / cell
150
100
50
0
control
lrrcc1 ATG
E
Actin signal
**
Mean signal intensity / cell
200
150
100
50
0
control
ccdc61 Spl

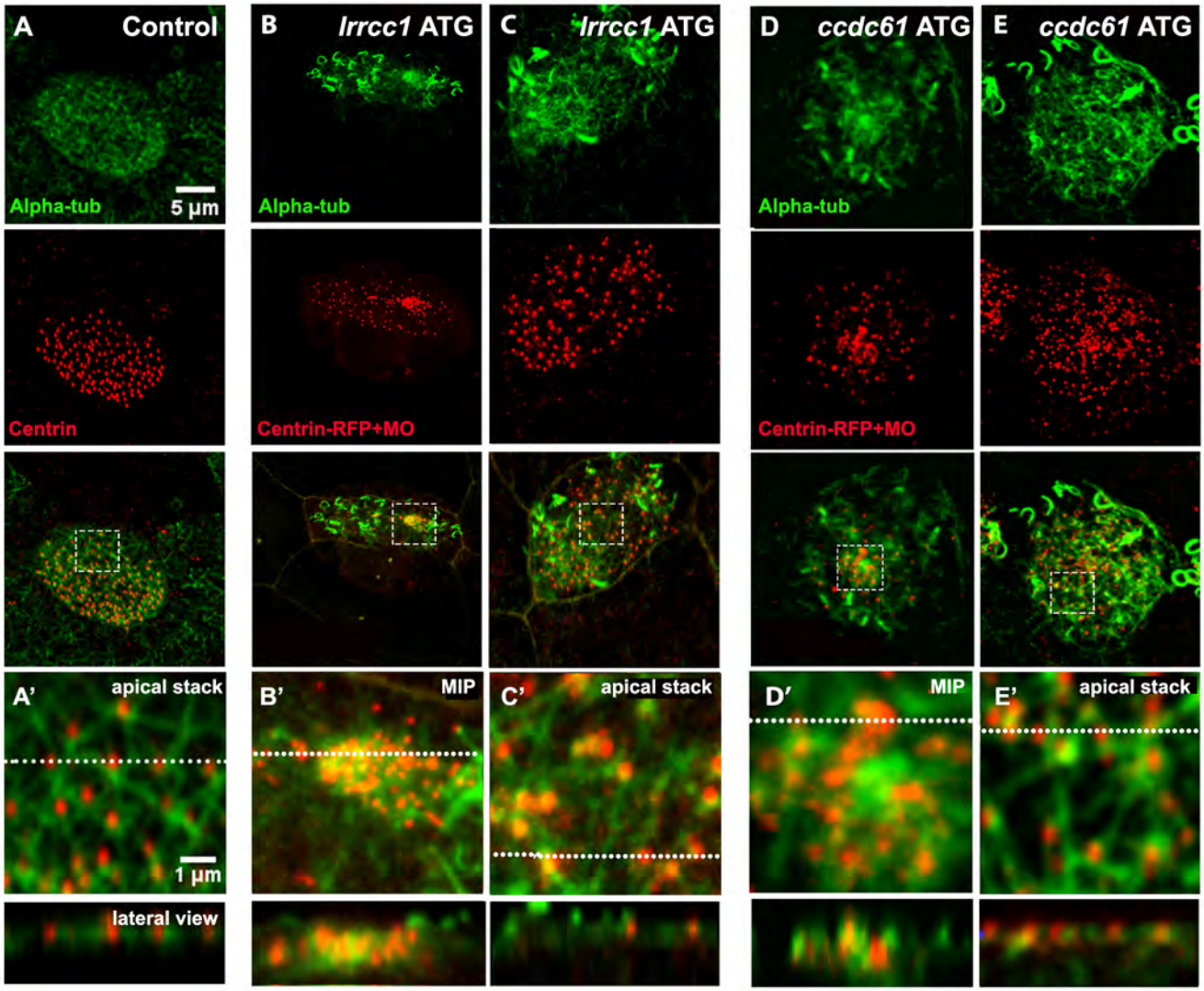
A Control
B lrrcc1 ATG
C lrrcc1 ATG
D ccdc61 ATG
E ccdc61 ATG
Alpha-tub
5 µm
Alpha-tub
Alpha-tub
Centrin
Centrin-RFP+MO
Centrin-RFP+MO
A'
apical stack
B'
MIP
C'
apical stack
D'
MIP
E'
apical stack
1 µm
lateral view

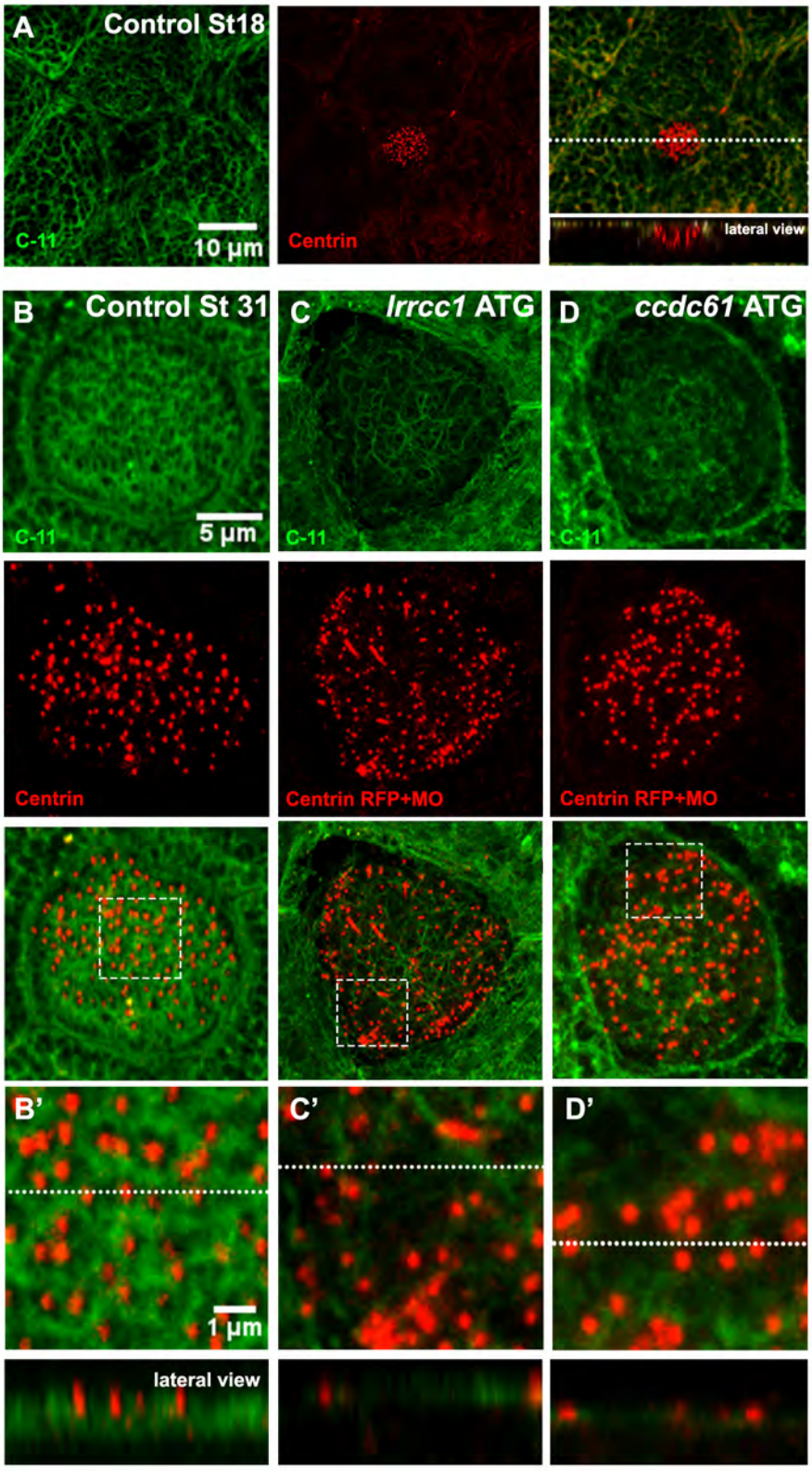
A
Control St18
C-11
10 µm
Centrin
lateral view
B
Control St 31
C-11
5 µm
C
lrrcc1 ATG
C-11
D
ccdc61 ATG
C-11
Centrin
Centrin RFP+MO
Centrin RFP+MO
B'
1 µm
C'
D'
lateral view

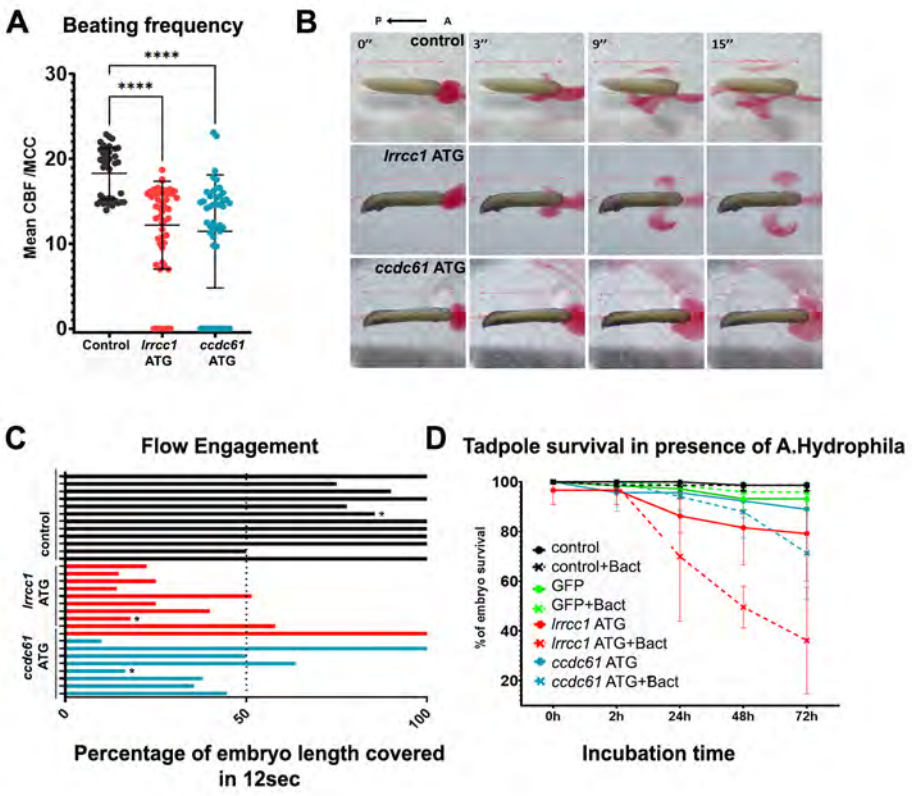
A
Beating frequency
****
****
Mean CBF /MCC
30
20
10
0
Control
lrrcc1 ATG
ccdc61 ATG
B
P
A
0"
control
3"
9"
15"
lrrcc1 ATG
ccdc61 ATG
C
Flow Engagement
control
lrrcc1 ATG
ccdc61 ATG
0
50
100
Percentage of embryo length covered in 12sec
D
Tadpole survival in presence of A.Hydrophila
%of embryo survival
100
80
60
40
20
control
control+Bact
GFP
GFP+Bact
lrrcc1 ATG
lrrcc1 ATG+Bact
ccdc61 ATG
ccdc61 ATG+Bact
0h
2h
24h
48h
72h
Incubation time

Nommick et al.

Supplementary material

Movie legends

Movie 1: Examples of Lrrcc1 and Ccdc61 morphant MCCs with partially preserved ciliary beating

Cilia beating was recorded at 250 fps, and the video is played at 50 fps to better appreciate cilia movement.

Movie 2: Examples of Lrrcc1 and Ccdc61 morphant MCCs without ciliary beating

Cilia beating was recorded at 250 fps, and the video is played at 50 fps to better appreciate cilia movement.

Movie 3: Analysis of fluid flow in control, Lrrcc1 and Ccdc61 morphant embryos

The video is played at real speed. Timing started when red microspheres were deposited onto the embryos.

Supplementary figure legends

Figure S1. *lrrcc1* and *ccdc61* expression in *Xenopus laevis* embryos.

(A) *In-situ* hybridization for *lrrcc1* and *ccdc61* at St 20. (B) Fluorescent *In-situ* hybridization for *lrrcc1* or *ccdc61* (green) and *α-tubulin* (red) at St 20. (C) ClearVolume 3D top and lateral views of a single BB, showing the localization of γ-Tubulin (white), relative to Clamp-GFP (green), and Centrin (red). (D) MIPs (maximum intensity projections) of confocal acquisitions of MCCs showing Lrrcc1-GFP (green) and Centrin (red) localization. Dashed white line sets the position of the lateral view. White arrow on the magnification indicates the BB analyzed by ClearVolume in E. (F, G) MIPs of confocal acquisitions of MCCs showing Ccdc61-GFP (green), Centrin (red) and γ-Tubulin (white) localization.

Dashed white line sets the position of the lateral view. White arrow on the magnification in G indicates the BB analyzed by ClearVolume below. White dashed boxes indicate higher magnification views.

Figure S2. Lrrcc1 and Ccdc61 morpholino-mediated knock-down

(A) Schematic representation of *Xenopus lrrcc1* and *ccdc61* pre-mRNAs with introns and exons relative position and size. Red bars below exon1 show the position of *ccdc61* and *lrrcc1* MO ATG and Spl. (B) MIPs of confocal acquisitions of St31 control or morphant MCCs stained for Centrin (centrioles, red), Lrrcc1 (green) and mRFP (tracer co-injected with MO, white). MO efficiency is validated by disappearance of the immunofluorescent signal. (C) MIPs of confocal acquisitions of St 31 control or morphant MCCs expressing Ccdc61-GFP (green) and stained for Centrin (red) and mRFP (tracer co-injected with MO, white). MO efficiency is validated by extinction of Ccdc61-GFP. (D) Quantification of signal intensity of Lrrcc1 immunofluorescence or Ccdc61-GFP in presence or absence of MO (number of MCCs analyzed: control=44, *lrrcc1* ATG/*lrrcc1* Spl/Ccdc61-GFP mosaic embryos=44/116/53, *lrrcc1* ATG-MO=39, *lrrcc1* Spl-MO=76, *ccdc61* ATG-MO=58, from 2 independent experiments). Each point represents an MCC. Horizontal lines represent the mean and SD. When the data followed a normal distribution, we compared them with Student t-test, and if not, with Mann-Whitney test. For all graphs $p = 0.0001 - 0.001$ or <0.0001 (***), $p = 0.001 - 0.01$ (**); $p = 0.01 - 0.05$ (*) and $p = \geq 0.05$ not significant (ns). (E-F) Western Blots of non-injected (NI), Lrrcc1/Ccdc61-GFP and Lrrcc1-GFP+MO/Ccdc61-GFP+MO injected embryos. PCNA was used as loading control. (G) Quantification of GFP expression from Western Blot (E, F) by densitometry using Image J software. Protein level expression was normalized with respect to the loading control protein PCNA.

Figure S3. Lrrcc1 and Ccdc61 knockdown impairs BB docking, spacing and orientation

(A) MIPs of confocal acquisitions of MCCs from St 31 control, Lrrcc1 Spl or Ccdc61 Spl morphant embryos stained with Centrin Ab, or Centrin-RFP co-injected with MOs (red). Dashed lines set the position of the corresponding lateral views presented below. (B) Graph displaying the apico-basal (A-B) distribution of centrioles within control, Lrrcc1 and Ccdc61 morphant and rescued (+mRNA) MCCs. Each point represents the maximum depth at which centrioles have been observed in each MCC.

Horizontal lines represent the mean and SD (number of MCCs analyzed: control=28, *lrrcc1* Spl-MO with/without mRNA=33/35, *ccdc61* Spl-MO with/without mRNA=28/29, from 3 independent experiments) (C) MIPs of confocal acquisitions of apical BBs in MCCs from St 31 control, Lrrcc1 or Ccdc61 morphant embryos stained with Centrin Ab or Centrin-RFP co-injected with MOs (red) and Delaunay triangulation (see methods) outputs (bottom row). Each colour is associated to a range of triangle areas in pixel^2. (D) Violin plots displaying the distribution of triangle areas in μm^2 of control, morphant and rescued MCCs. The horizontal line indicates the median, dashed lines indicate the quartiles (number of MCCs analyzed: control=19, *lrrcc1* Spl-MO with/without mRNA=28/27, *ccdc61* Spl-MO with/without mRNA=11/28, from 3 independent experiments). (E) MIPs of confocal acquisitions of control and morphant MCCs stained with Centrin (red, centrioles) and γ-Tubulin (white, BF). At the right corner of each MIP, magnifications of the same MCCs are shown to appreciate BB orientation. Below each cell, its respective rose histogram representing the distribution of BB orientations. The black line running from the centre of the diagram to the outer edge is the mean angle and the arcs extending to either side represent the confidence limits of the mean (when the mean angle is only theoretical but not significant, the line turns pink). (F) Circular Standard Deviations of control, morphant and rescued MCCs. Each point represents a single cell. Horizontal lines represent the mean and SD (number of MCCs analyzed: control=125, *lrrcc1* Spl-MO with/without mRNA=28/45, *ccdc61* Spl-MO with/without mRNA=27/20, from 3 independent experiments). (G) Graph displaying the percentage of non-polarized MCCs (no significant mean angle of BBs within a cell can be calculated), as revealed by the Rayleigh statistical test (number of MCCs analyzed: control=591, *lrrcc1* Spl-MO=33, *ccdc61* Spl-MO=159, from 3 independent experiments). All confocal images are at the scale shown in (A). When the data followed a normal distribution, we compared them with one One-way ANOVA, and if not, with Kruskal-Wallis test. For all graphs p = 0.0001 - 0.001 or <0.0001 (***), p = 0.001 - 0.01 (**); p = 0.01 - 0.05 (*) and p = ≥0.05 not significant (ns).

Figure S4. Correct BB organization is rescued upon Lrrcc1-GFP and Ccdc61-GFP mRNA co-injection in morphant MCCs.

(A) MIPs of confocal acquisitions of St 31 control and morphant MCCs stained for centrioles (Centrin Ab, red), cilia (Acetylated-α-tubulin Ab, green) and morpholino tracer (mRFP co-injected with MOs, white). White dashed lines indicate morphant MCCs. Note that ciliogenesis is preserved in morphant MCCs. (B-E) Embryos were sequentially injected first with MO + Centrin-RFP and then with Lrrcc1-GFP or MOresCcdc61-GFP mRNA (green). (B, D) MIPs of confocal acquisitions of St 31 MCCs expressing Centrin-RFP (BBs, tracer for MO injection, red), immunostained for BF (γ-tubulin, white). The absence of specific signal in the green channel identifies those cells as morphant MCCs, consistent with severe BB disorganization. (C, E) MIPs of confocal acquisitions of MCCs expressing Centrin-RFP co-injected with MOs (red), Lrrcc1-GFP or MOresCcdc61-GFP (green) and immunostained for BF (white). In GFP-positive morphant MCCs, BB organization is largely rescued and comparable to control (see Fig. 2 and S3). White dashed boxes in C and E indicate higher magnification views. All confocal images are at the scale shown in (B). At the right border of C and E, single slice magnified views are shown to better appreciate Lrrcc1-GFP and MOres Ccdc61-GFP localization (green) with respect to basal bodies.

Figure S5. Pericentrin antibody validation.

(A) Schematic representation of *Xenopus laevis* Pcnt protein. A portion of the protein between aa 3340-3643 was used as immunogen to generate rabbit polyclonal antibody. (B) COS-1 cells were transfected or not (control) with vectors coding for the indicated proteins and immunoblotted with custom-made Pcnt rabbit Ab, or Ab against GFP. The expected size of GFP-Pcnt is 62 kDa.

Figure S6. Deciliation of *Xenopus* epidermal MCCs

MIPs of confocal acquisitions of the ciliated epidermis before and after dibucaine treatment. Cilia and MTs are stained with α-Tubulin Ab (green). The absence of cilia upon dibucaine treatment allows the observation of cytoplasmic MTs. White dotted boxes indicate higher magnification views shown below.

Figure S7. Phenotype validation of embryos incubated with *A. hydrophila*.

MIPs of confocal acquisitions of epidermis of St 31 embryos, from the same experimental pool as those used for our survival assay (Fig. 7), stained for cilia (α-Tubulin Ab, green), centrioles (Centrin Ab, white) and MO tracer (mRFP Ab, red). The visible BB disorganization confirms MO efficiency.

Supplementary Tables

Gene name (bait)	Gene Name (prey)	Enrichment	Linked to centriole/cilia/MTs	Found in *Xenopus* MCCs
LRRCC1	LRRCC1	10,59121	YES	YES
LRRCC1	CCDC77	9,79952	PROBABLE	YES
LRRCC1	AZI1/CEP131	9,645587	YES	?
LRRCC1	PCM1	8,385486	YES	YES
LRRCC1	CEP72	8,169336	YES	YES
LRRCC1	MIB1	6,578583	YES	NO
LRRCC1	FOPNL/FOR20/CEP20	6,448221	YES	YES
LRRCC1	BBS4	6,426498	YES	YES
LRRCC1	OFD1	6,392701	YES	YES
LRRCC1	WDR90	6,318789	YES	YES
LRRCC1	KIAA0753/OFIP	6,241836	YES	YES
LRRCC1	CSPP1	6,139616	YES	YES
LRRCC1	KIAA1731/CEP295	5,889853	YES	YES
LRRCC1	PIBF1	5,812087	YES	YES
LRRCC1	CCDC18	5,503085	PROBABLE	YES
LRRCC1	WDR67	4,986441	YES	?
LRRCC1	CCDC61	4,976773	YES	YES
LRRCC1	FGFR1OP/CEP43	4,853146	YES	YES
LRRCC1	SSX2IP	4,807299	YES	yes
LRRCC1	CCDC14	4,215897	YES	YES
LRRCC1	KIAA1328	3,94653	YES	NO
LRRCC1	CEP350	3,833714	YES	YES
LRRCC1	PHLDB2	3,801527	YES	NO
LRRCC1	PRKAR2A	3,785393	YES	NO
LRRCC1	TTLL5	3,725921	YES	NO
LRRCC1	N4BP3	3,684075	NO	?
LRRCC1	CEP170	2,879607	YES	YES
LRRCC1	ESCO2	2,533443	NO	?
LRRCC1	SPICE1	2,417896	YES	YES
LRRCC1	KIFC3	2,255614	YES	NO
FGFR1OP	CCDC61	7,169243	YES	YES
CEP120	CCDC61	7,155219	YES	YES

OFD1	CCDC61	5,799062	YES	YES
CEP72	CCDC61	5,62468	YES	YES
MIB1	CCDC61	5,100073	YES	NO
LRRCC1	CCDC61	4,976773	YES	YES
CEP135	CCDC61	4,941259	YES	YES
SDCCAG8	CCDC61	4,656678	YES	YES
CEP152	CCDC61	4,148394	YES	YES
KIF7	CCDC61	3,749279	YES	NO
TPX2	CCDC61	3,734188	YES	NO
NEDD1	CCDC61	3,682512	YES	YES
CEP55	CCDC61	3,550385	YES	NO
CCDC14	CCDC61	3,546823	YES	YES
SLAIN2	CCDC61	3,535149	YES	NO
PPP2CB	CCDC61	3,320352	NO	NO
PCM1	CCDC61	3,265138	YES	YES
AZI1/CEP131	CCDC61	2,932961	YES	?
CSNK1E	CCDC61	2,845102	NO	NO
ANKRD26	CCDC61	2,78639	YES	YES
PRKAR2A	CCDC61	2,684373	YES	NO
PPP2R5D	CCDC61	2,613387	NO	?
ZBTB33	CCDC61	2,575864	NO	NO
RAD54L	CCDC61	1,843647	NO	NO
SRPR	CCDC61	1,821545	NO	NO

Table S1: Lrrcc1 and Ccdc61 interactors

This table has been annotated from the Human Interactome Purification and Mass Spectrometry data of Hein et al., (2015). In green are shown common interactors between Lrrcc1 and Ccdc61. Enrichment values represent the average enrichment of the protein in multiples of standard deviations compared to control samples. Published evidence was screened to identify the existence or not of links with centrioles, cilia or MTs. Transcript expression in *Xenopus* tropicalis MCCs is displayed, as revealed by scRNA-sequencing (Briggs et al., 2018). Question marks correspond to transcripts that were totally absent from the available dataset.

mRNA	**Quantity injected per blastomere (pg)**	**Stage of injection**
lrrcc1-GFP	300	8/16 cells

ccdc61-GFP	300	8/16 cells
mRFP	200	4/8 cells
centrin-RFP	50	4/8 cells
GFP-gpi	500	4/8 cells

Table S2 : mRNA injection conditions

Fixation	Target/Species/Isotype	Reference	Dilution
MetOH 100% 4°C over weekend or PFA 4% 0,1% Triton 30min RT	γ-Tubulin mouse IgG1	Abcam Ab11316	1/800
	Acetylated-tubulin mouse IgG2b	Sigma-Aldrich T7451	1/1000
	GFP chicken	AvesLab GFP-1020	1/500
	RFP rat IgG2a	Chromotek 5F8	1/500
	Centrin mouse IgG2a	Sigma-Aldrich 04-1624	1/1000
	Cytokeratin (Pan-reactive) mouse monoclonal IgG1	Sigma-Aldrich SAB4700666	1/500
	Z01 mouse IgG1	Thermo Scientifique 33-9100	1/200
	α-Tubulin mouse IgG1	Sigma-Aldrich T9026	1/500
Memfa 1h RT	Sir-Actin	Spirochrome SC001	1/1000
Memfa 2h RT or overnight 4C°C	Anti-DIG-PA conjugated IgG	Roche 11266026	1/500
PFA 4% Triton 0,1x 30min RT	Pericentrin rabbit	Home made, this study	1/5000
MetOH 100% -20°C over weekend	Lrrcc1 rabbit polyclonal (immunofluorescence)	Sigma-Aldrich HPA012893	1/1000
PFA 4% 0,1% Triton 30min RT	Lrrcc1 rabbit polyclonal (MO validation)	Gaudin et al., 2021 bioRxiv DOI: https://doi.org/10.1101/2021.07.21.453218	1/100
MetOH 100% -20°C over weekend	Ccdc61 rabbit polyclonal	Pizon et al., 2020	1/500
Western Blot	PCNA mouse monoclonal	Sigma-Aldrich P8825	1/5000
Western Blot	GFP Sheep polyclonal	MRC PPU reagent, University of Dundee, UK, #S268	1/2000

Table S3: Primary antibodies and markers

Antibody	Reference	Dilution
Alexa anti mouse IgG2a 488	Invitrogen Thermo Fisher A21131	1/800
Alexa anti mouse IgG2a 568	Invitrogen Thermo Fisher A21134	1/800
Alexa anti mouse IgG2a 647	Invitrogen Thermo Fisher A21241	1/800
Alexa anti mouse IgG1 488	Invitrogen Thermo Fisher A21121	1/800
Alexa anti mouse IgG1 568	Invitrogen Thermo Fisher A21124	1/800
Alexa anti mouse IgG1 647	Invitrogen Thermo Fisher A21240	1/800
Alexa anti mouse IgG2b 488	Invitrogen Thermo Fisher A21141	1/800
Alexa anti mouse IgG2b 568	Invitrogen Thermo Fisher A21144	1/800
Alexa anti mouse IgG2b 647	Invitrogen Thermo Fisher A21242	1/800
Anti rat Cy3 IgG	Jackson ImmunoResearch 712165153	1/500
Alexa fluor Anti rat 488 IgG	Life Technologies A21208	1/500
Alexa fluor Anti rat 647 IgG	Jackson ImmunoResearch 712605153	1/500
Alexa fluor Anti rabbit 488 IgG	Life Technologies A21206	1/500
Alexa fluor Anti rabbit 568 IgG	Life Technologies A10042	1/500
Alexa fluor Anti rabbit 647 IgG	Life Technologies A31573	1/500
Alexa fluor Anti chicken 488 IgY	Jackson ImmunoResearch 703545155	1/500

Table S4: Secondary antibodies

Experiment	Condition	Number of MCCs (or BBs for TEM) analyzed	Number of embryos analyzed per condition	Number of experimental repeats
BB orientation	control	125	4-9	2-3
	lrrcc1 ATG-MO	24		
	lrrcc1 Spl-MO	28		
	ccdc61 ATG-MO	33		
	ccdc61 Spl-MO	27		
	lrrcc1 ATG-MO +mRNA	40		
	lrrcc1 Spl-MO +mRNA	45		
	ccdc61 ATG-MO +mRNA	39		
	ccdc61 Spl-MO +mRNA	20		

MCC polarization **Rayleigh Test**	control	591	4-9	3
	lrrcc1 ATG-MO	181		
	lrrcc1 Spl-MO	33		
	ccdc61 ATG-MO	158		
	ccdc61 Spl-MO	159		
BB docking	control	28	3-9	2-3
	lrrcc1 ATG-MO	36		
	lrrcc1 Spl-MO	33		
	ccdc61 ATG-MO	34		
	ccdc61 Spl-MO	28		
	lrrcc1 ATG-MO +mRNA	41		
	lrrcc1 Spl-MO +mRNA	35		
	ccdc61 ATG-MO +mRNA	35		
	ccdc61 Spl-MO +mRNA	29		
BB spacing	control	19	2-3	2
	lrrcc1 ATG-MO	20		
	lrrcc1 Spl-MO	28		
	ccdc61 ATG-MO	27		
	ccdc61 Spl-MO	11		
	lrrcc1 ATG-MO +mRNA	43		
	lrrcc1 Spl-MO +mRNA	27		
	ccdc61 ATG-MO +mRNA	28		
	ccdc61 Spl-MO +mRNA	28		
Actin signal	control (of *lrrcc1* ATG)	72	3	2
	control (of *lrrcc1* Spl)	43		
	lrrcc1 ATG-MO	31		
	ccdc61 Spl-MO	32		
Flow engagement	control		12	2
	lrrcc1 ATG-MO		10	
	ccdc61 ATG-MO		8	
Cilia beating	control	39	13	2
	lrrcc1 ATG-MO	49	17	

	ccdc61 ATG-MO	47	15	
Pericentrin signal	control (of lrrcc1)	91	5-9	2-3
	lrrcc1 ATG-MO	136		
	control (of ccdc61)	46		
	cdcd61 ATG-MO	143		
Rootlet presence (TEM)	control	134	2-3	1-2
	lrrcc1 ATG-MO	174		
	ccdc61 ATG-MO	120		
Embryo survival in presence of bacteria	control		73	3
	control+BACT		84	
	GFP		73	
	GFP +BACT		74	
	lrrcc1 ATG-MO		45	
	lrrcc1 ATG +BACT		53	
	ccdc61 ATG-MO		35	
	ccdc61 ATG +BACT		38	
Morpholino validation by immunostaining	control (*lrrcc1* ATG)	44	5-7	2
	control (*lrrcc1* Spl)	116		
	control (Ccdc61-GFP)	53		
	lrrcc1 ATG-MO	39		
	lrrcc1 Spl-MO	76		
	ccdc61 ATG-MO	58		

Table S5 : Experimental replicates and sample sizes

Fig.S1

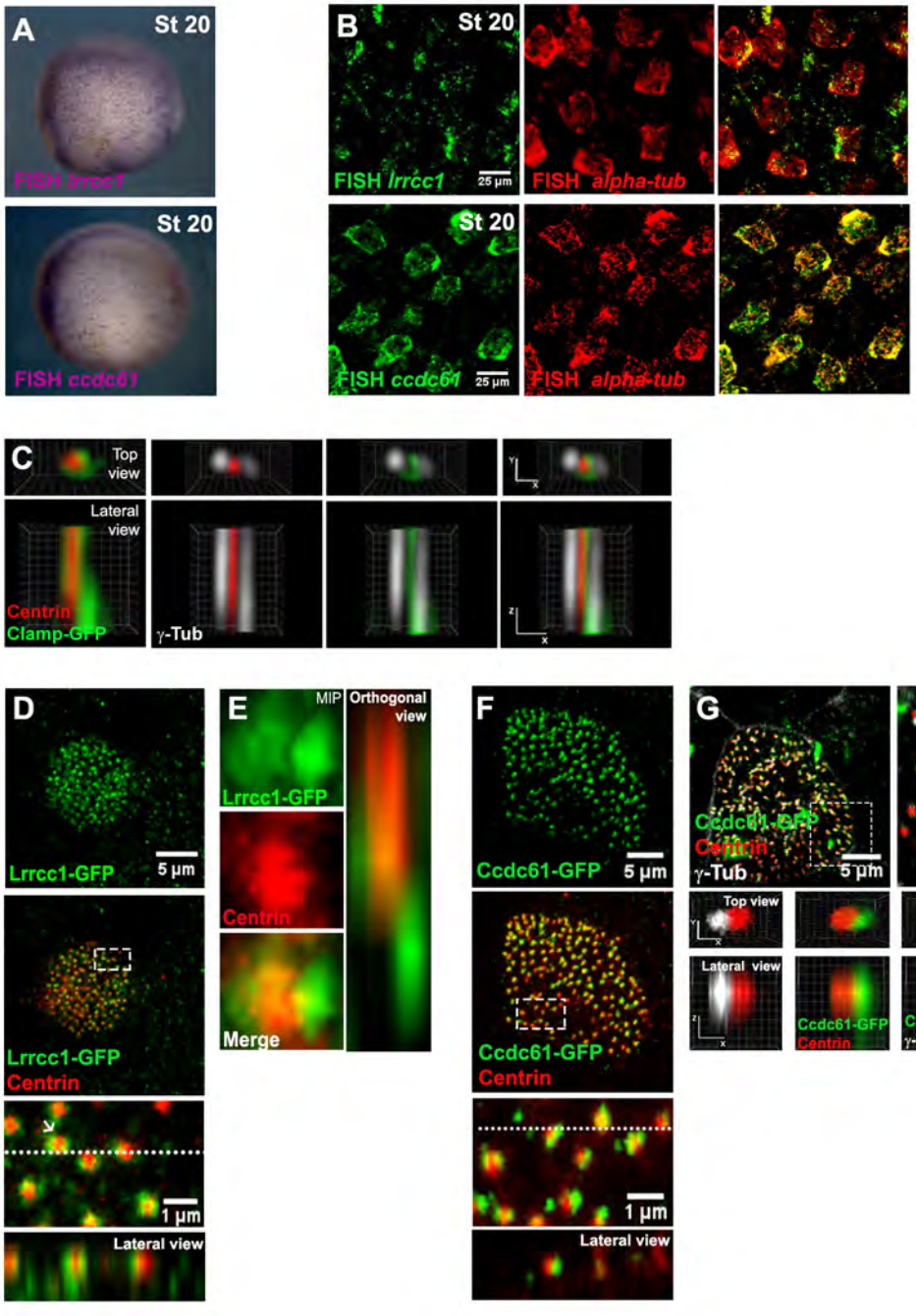
A
St 20
FISH lrrcc1
St 20
FISH ccdc61
B
St 20
FISH lrrcc1
25 µm
FISH alpha-tub
St 20
FISH ccdc61
25 µm
FISH alpha-tub
C
Top view
Lateral view
Centrin
Clamp-GFP
γ-Tub
D
Lrrcc1-GFP
5 µm
Lrrcc1-GFP
Centrin
1 µm
Lateral view
E
MIP
Orthogonal view
Lrrcc1-GFP
Centrin
Merge
F
Ccdc61-GFP
5 µm
Ccdc61-GFP
Centrin
1 µm
Lateral view
G
Ccdc61-GFP
Centrin
γ-Tub
5 µm
Top view
Lateral view
Ccdc61-GFP
Centrin
Ccdc61-GFP
γ-Tub

Fig.S2

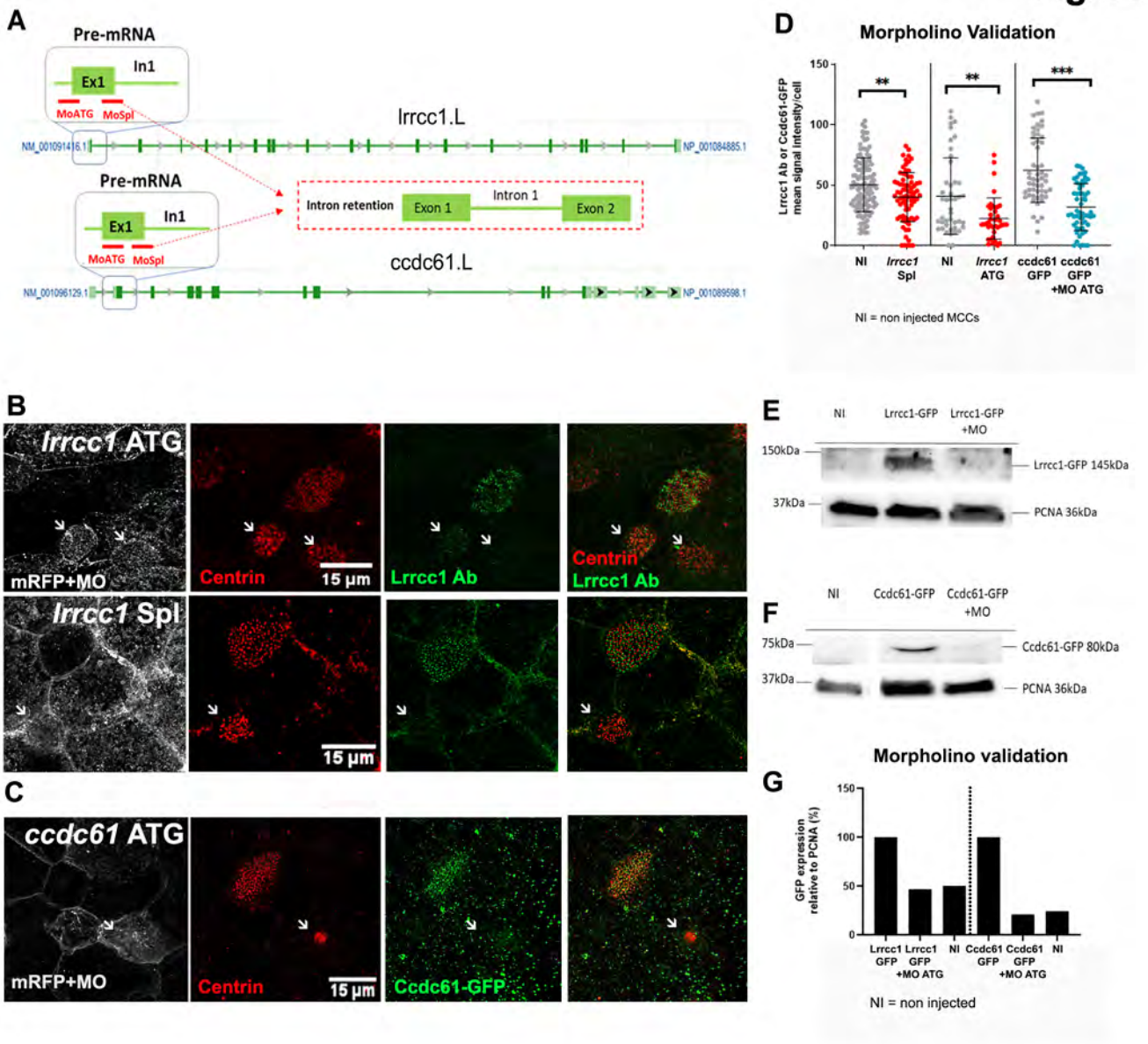
A
Pre-mRNA
In1
Ex1
MoATG
MoSpl
lrrcc1.L
NM_001091416.1
NP_001084885.1
Pre-mRNA
In1
Ex1
MoATG
MoSpl
Intron retention
Exon 1
Intron 1
Exon 2
ccdc61.L
NM_001096129.1
NP_001089598.1
B
lrrcc1 ATG
mRFP+MO
Centrin
15 µm
Lrrcc1 Ab
Centrin
Lrrcc1 Ab
lrrcc1 Spl
15 µm
C
ccdc61 ATG
mRFP+MO
Centrin
15 µm
Ccdc61-GFP
D
Morpholino Validation
Lrrcc1 Ab or Ccdc61-GFP mean signal intensity/cell
150
100
50
0
**
**
***
NI
lrrcc1 Spl
NI
lrrcc1 ATG
ccdc61 GFP
ccdc61 GFP +MO ATG
NI = non injected MCCs
E
NI
Lrrcc1-GFP
Lrrcc1-GFP +MO
150kDa
Lrrcc1-GFP 145kDa
37kDa
PCNA 36kDa
F
NI
Ccdc61-GFP
Ccdc61-GFP +MO
75kDa
Ccdc61-GFP 80kDa
37kDa
PCNA 36kDa
G
Morpholino validation
GFP expression relative to PCNA (%)
150
100
50
0
Lrrcc1 GFP
Lrrcc1 GFP +MO ATG
NI
Ccdc61 GFP
Ccdc61 GFP +MO ATG
NI
NI = non injected

Fig.S3

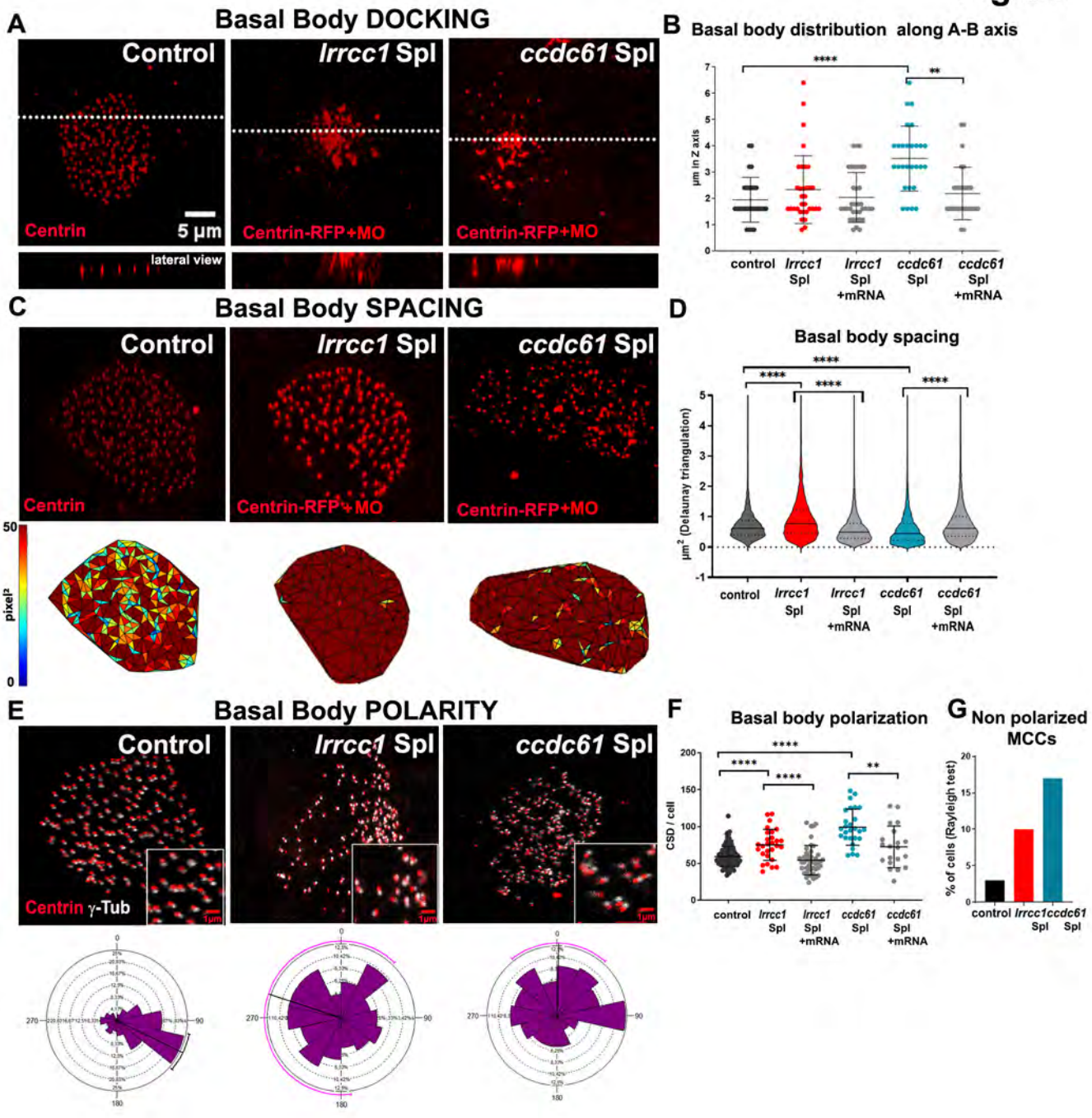
A
Basal Body DOCKING
Control
lrrcc1 Spl
ccdc61 Spl
Centrin
5 µm
Centrin-RFP+MO
Centrin-RFP+MO
lateral view
B
Basal body distribution along A-B axis
µm in Z axis
control
lrrcc1 Spl
lrrcc1 Spl +mRNA
ccdc61 Spl
ccdc61 Spl +mRNA
C
Basal Body SPACING
Control
lrrcc1 Spl
ccdc61 Spl
Centrin
Centrin-RFP+MO
Centrin-RFP+MO
pixel²
50
0
D
Basal body spacing
µm² (Delaunay triangulation)
E
Basal Body POLARITY
Control
lrrcc1 Spl
ccdc61 Spl
Centrin γ-Tub
F
Basal body polarization
CSD / cell
G
Non polarized MCCs
% of cells (Rayleigh test)

Fig.S4

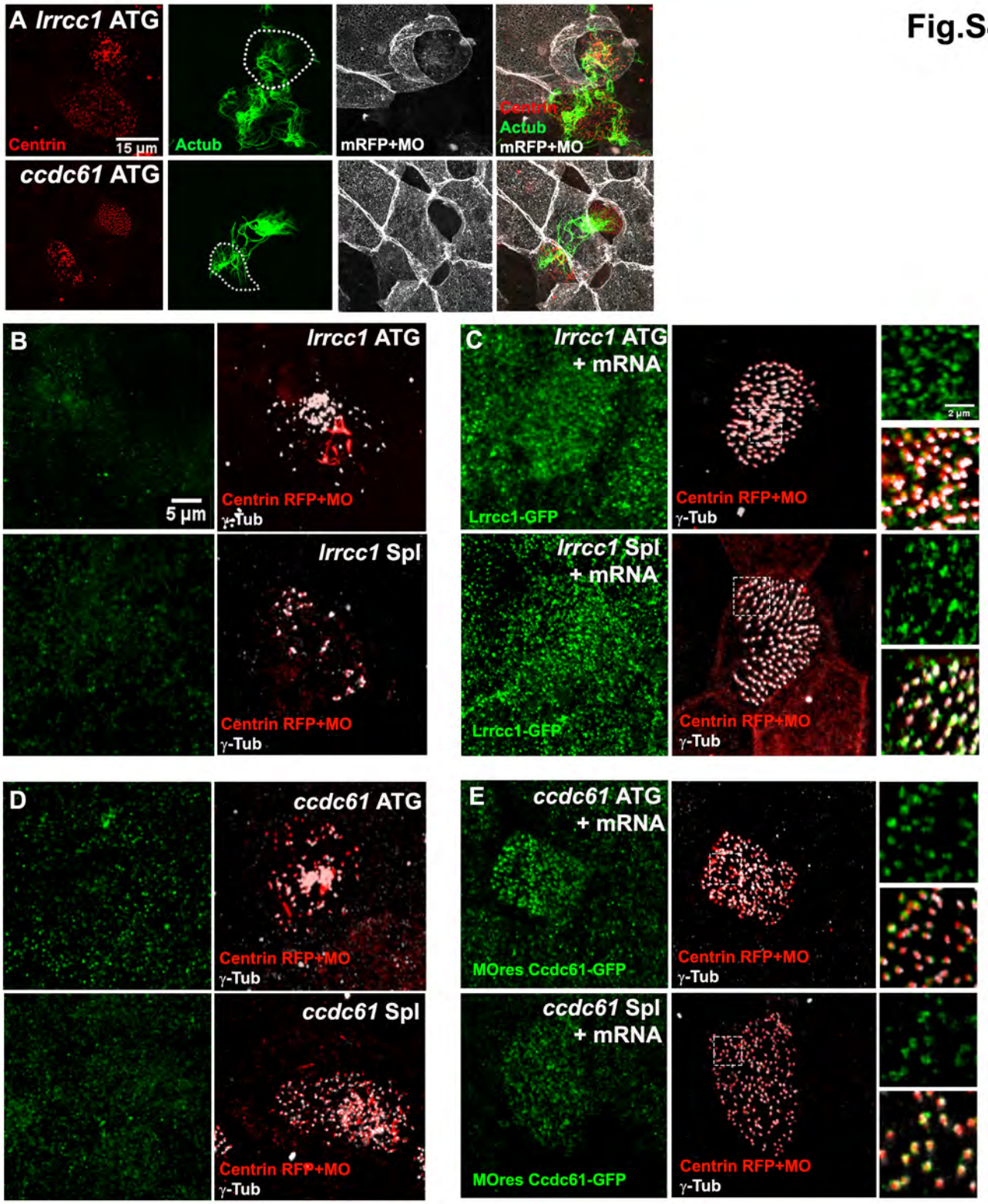
A lrrcc1 ATG
Centrin
15 µm
Actub
mRFP+MO
Centrin
Actub
mRFP+MO
ccdc61 ATG
B
lrrcc1 ATG
5 µm
Centrin RFP+MO
γ-Tub
lrrcc1 Spl
Centrin RFP+MO
γ-Tub
C
lrrcc1 ATG
+ mRNA
Lrrcc1-GFP
Centrin RFP+MO
γ-Tub
2 µm
lrrcc1 Spl
+ mRNA
Lrrcc1-GFP
Centrin RFP+MO
γ-Tub
D
ccdc61 ATG
Centrin RFP+MO
γ-Tub
ccdc61 Spl
Centrin RFP+MO
γ-Tub
E
ccdc61 ATG
+ mRNA
MOres Ccdc61-GFP
Centrin RFP+MO
γ-Tub
ccdc61 Spl
+ mRNA
MOres Ccdc61-GFP
Centrin RFP+MO
γ-Tub

Fig.S5

A


Xenopus laevis Pcnt (4489aa)
Immunogen
(aa 3340-3643)

B

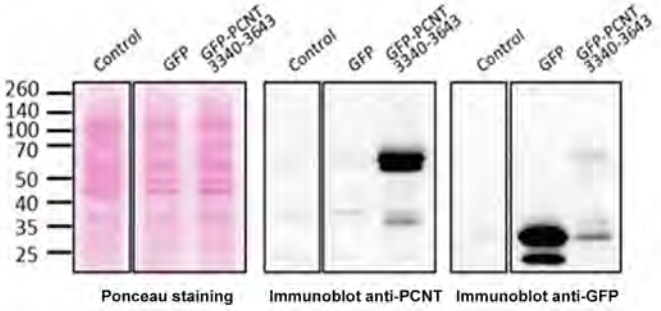
Control
GFP
GFP-PCNT 3340-3643
260
140
100
70
50
40
35
25
Ponceau staining
Immunoblot anti-PCNT
Immunoblot anti-GFP

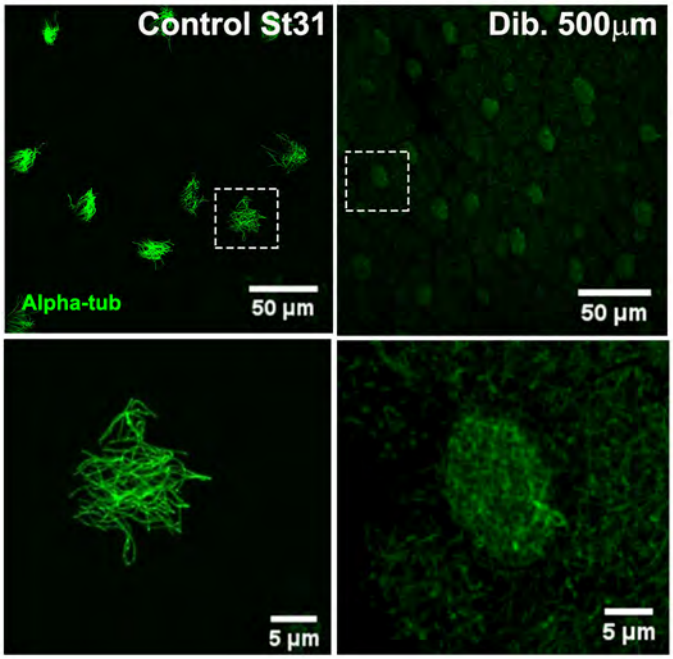

Fig.S6

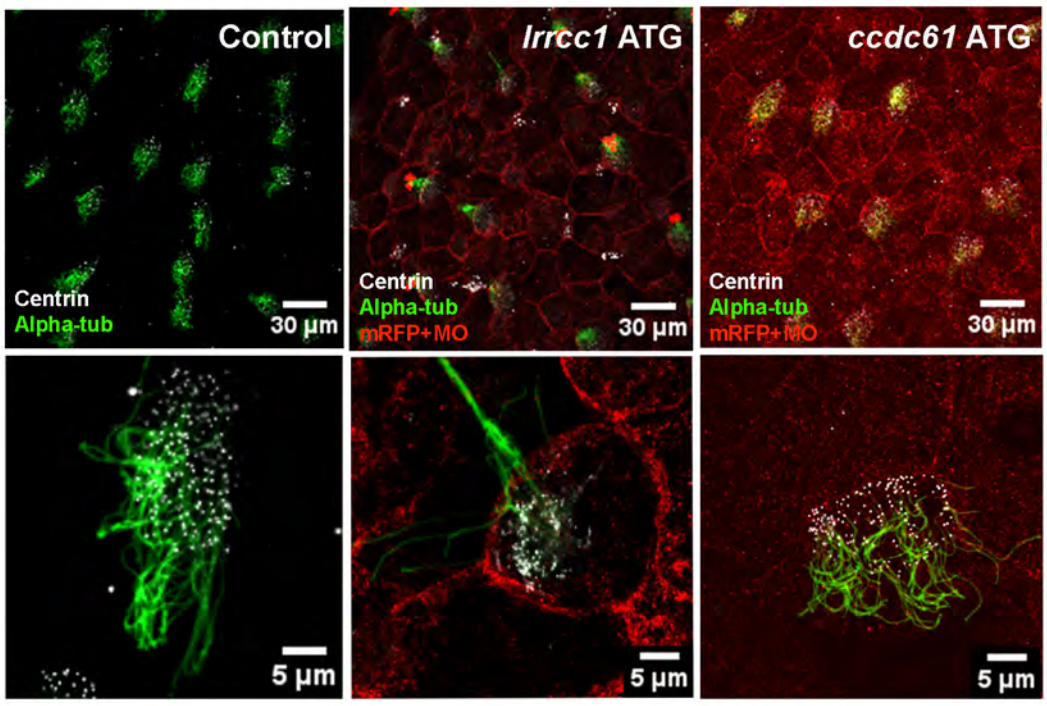
Control
Centrin
Alpha-tub
30 μm
lrrcc1 ATG
Centrin
Alpha-tub
mRFP+MO
30 μm
ccdc61 ATG
Centrin
Alpha-tub
mRFP+MO
30 μm
5 μm
5 μm
5 μm

Fig.S7